

## CHANDRA'S CLOSE ENCOUNTER WITH THE DISINTEGRATING COMETS 73P/2006 (SCHWASSMANN-WACHMANN 3) FRAGMENT B AND C/1999 S4 (LINEAR)

S. J. WOLK<sup>1</sup>, C. M. LISSE<sup>2</sup>, D. BODEWITS<sup>3,6</sup>, D. J. CHRISTIAN<sup>4</sup>, AND K. DENNERL<sup>5</sup>

<sup>1</sup> Harvard-Smithsonian Center for Astrophysics, 60 Garden Street, Cambridge, MA 02138, USA

<sup>2</sup> Planetary Exploration Group, Space Department, Johns Hopkins University Applied Physics Laboratory, 11100 Johns Hopkins Rd., Laurel, MD 20723, USA

<sup>3</sup> KVI Atomic Physics, University of Groningen, Zernikelaan 25, NL-9747 AA Groningen, Netherlands

<sup>4</sup> Eureka Scientific Inc., 2452 Delmar St., Oakland, CA 94602, USA

<sup>5</sup> Max-Planck-Institut für extraterrestrische Physik, Giessenbachstraße, 85748 Garching, Germany

Received 2008 May 23; accepted 2009 January 5; published 2009 March 24

### ABSTRACT

On 2006 May 23, we used the ACIS-S instrument on *Chandra* to study the X-ray emission from the B fragment of comet 73P/2006 (Schwassmann-Wachmann 3) (73P/B). We obtained a total of 20 ks of *Chandra* observation time of Fragment B, and also investigated contemporaneous *Advanced Composition Explorer* and *Solar and Heliospheric Observatory* solar wind physical data. The *Chandra* data allow us to spatially resolve the detailed structure of the interaction zone between the solar wind and the fragment's coma at a resolution of  $\sim 1000$  km, and to observe the X-ray emission due to multiple comet-like bodies. We detect a change in the spectral signature with the ratio of the C V/O VII line increasing with increasing collisional opacity as predicted by Bodewits et al. The line fluxes arise from a combination of solar wind speed, the species that populate the wind, and the gas density of the comet. We are able to understand some of the observed X-ray morphology in terms of nongravitational forces that act upon an actively outgassing comet's debris field. We have used the results of the *Chandra* observations on the highly fragmented 73P/B debris field to reanalyze and interpret the mysterious emission seen from comet C/1999 S4 (LINEAR) on 2000 August 1, after the comet had completely disrupted. We find the physical situations to be similar in both cases, with extended X-ray emission due to multiple, small outgassing bodies in the field of view. Nevertheless, the two comets interacted with completely different solar winds, resulting in distinctly different spectra.

**Key words:** comets: individual (Schwassmann-Wachmann 3, Fragment B, Comet C/1999 S4) – solar wind – techniques: spectroscopic

**Online-only material:** color figures

### 1. INTRODUCTION

*ROSAT*'s discovery that comets are bright in X-rays has opened up a new window on solar system physics (Lisse et al. 1996, 2001; Dennerl et al. 1997; Dennerl 2002; McCammon et al. 2002; Pepino et al. 2004; Bhardwaj et al. 2007). By now, over 20 comets have been studied in X-rays and the physical emission process has been well identified (Cravens 1997; Krasnopolsky et al. 1997; Cravens 2002). Highly energetic solar wind ions (e.g.,  $O^{7+}$ ,  $O^{8+}$ ,  $C^{5+}$ ,  $C^{6+}$ ) collide with neutral particles in the comet's coma, resulting in charge exchange. For example, a solar wind  $O^{8+}$  ion captures one electron and results in O VIII emission. An  $O^{7+}$  ion captures one electron and leads to O VII emission.<sup>7</sup> The solar wind ions are left in an electronically excited state from which they decay through the emission of X-ray line photons (Bodewits et al. 2007). As solar wind ions gradually lose their charge by subsequent electron capture reactions, we expect charge exchange to occur in the Sunward direction relative to the comet with a strength related to the abundance of the neutral gas species available and the flux of the incident solar wind ions.

The details of the emission depend on the properties of both the solar wind (composition, charge state, density, and speed) and the comet's mass loss rate (Kharchenko & Dalgarno 2000, 2001; Beiersdorfer et al. 2003; Bodewits et al. 2004, 2007). Much effort has been expended in world-wide laboratories to measure these charge exchange cross sections and to develop cometary X-ray spectroscopy as a powerful tool to monitor the composition, charge state, density and speed of the solar wind as well as to probe comet activity (e.g., Beiersdorfer et al. 2003; Bodewits et al. 2004), but this work is still ongoing. In order to understand the solar wind–coma interaction, state selective cross sections and branching ratios are required to accurately model the de-excitation cascades of the different ions (Bodewits et al. 2007). This is challenging as the total cross sections and the population of specific excited states strongly depend on the collision energy and the species involved.

Periodic comets are small (0.5–10 km) bodies composed of a mixture of nonvolatile dust grains and frozen gasses, which traverse the solar system on elliptical orbits. As they approach the Sun, comets develop an atmosphere (coma) of sublimating neutral gases, mainly  $H_2O$ , CO (5%–20% versus  $H_2O$ ), and  $CO_2$  (1%–10% versus  $H_2O$ ) with trace amounts of other molecules. As these gasses expand away from the comet nucleus, solar UV photons and solar wind ions photodissociate and/or photoionize them on timescales of  $10^4$ – $10^7$  s (length scales of  $10^4$ – $10^7$  km) depending on the species. As the comet retreats from the Sun and the incident solar flux lessens in intensity, these time and length scales lengthen by the square of the heliocentric distance.

<sup>6</sup> Present address: NASA Postdoctoral Fellow, Goddard Space Flight Center, Solar System Exploration Division, Mailstop 690.3, Greenbelt, MD 20771, USA.

<sup>7</sup> In this paper, we are concerned with the output products of the interactions. Thus, ions with superscript notation are in the solar wind and ions that are emitting are notated in linear notation.

The solar wind interaction with comets is dominated by mass loading of the solar wind by heavy, slow cometary pickup ions (see a recent review by Ip 2004). The cometary ions are produced by photoionization and by charge exchange (Cravens 1991). The interaction begins outside the bow shock, which is the primary working surface of the interaction where the mass loading becomes large enough to change the macroscopic flow patterns of the solar wind. Also, such cometary ions are quickly removed by the solar wind. Models show that the interaction of the expanding coma with the solar wind results in the formation of a kidney-shaped region bounded by a contact surface and inner shock, where the dynamic pressure of the expanding cometary gasses balances the dynamic pressure of the solar wind (Kabin et al. 2000). Similar to the termination shock of the heliopause, this is the zone where the solar wind becomes highly mass loaded by picking up ionized local species (Gringauz et al. 1986).

The bow shock forms the outer boundary of this interaction region. Before X-ray observations became available, this complex interaction zone was poorly studied only along single chord trajectories through the coma by in situ energetic particle analyzers in three comets: 1P/1986 (Halley) (*Giotto*—Krankowsky et al. 1986; Vega 1 and 2—Galeev et al. 1986), 26P/Grigg-Skjellerup by *Giotto* (Johnstone et al. 1993), and 19P/Borrelly by DS-1 (Young et al. 2004). On the other hand, X-ray emission directly probes the entire interaction zone and hence both the macroscopic and microscopic processes that play a role in shaping of the coma and ion tails, as was demonstrated by Wegmann & Dennerl (2005).

Comet 73P/Schwassmann-Wachmann 3 (73P/2006) was a small short-period comet that broke up into several pieces in 1995 (Bohnhardt et al. 1995). Three main pieces (B, C, and E) survived this breakup to reappear during the 2006 apparition. Each of these pieces developed its own coma. The fragments further split into at least 43 major subcomponents (as tracked by JPL—see *Horizons*<sup>8</sup>) and literally thousands of other bodies too small to be detected, except during the initial flaring produced during their creation and ejection. Figure 1 shows a Hubble image of Fragment B. The fragments were found to have similar chemical compositions in their emitted gas and dust (Schleicher 2006; Villanueva et al. 2006; Dello Russo et al. 2007; M. Sitko et al. 2009, in preparation) but different mass loss rates, depending on their detailed structure. In terms of activity and outgassing, this comet was weak, comparable to Encke in 2003 November ( $Q_{\text{gas}} \sim 10^{28}$  mol s<sup>-1</sup>; Lisse et al. 2005; Wegmann et al. 2004). On the other hand, 73P/B had an extremely close approach to Earth in 2006 May (0.07 AU), about a factor of 5 closer than Encke in 2003. Due to its high activity at the time—it was in outburst during May—Fragment B was one of the two brightest fragments of the comet 73P/2006 debris train. The *Hubble Space Telescope* (*HST*) image (Figure 1) shows a structure analogous to comet C/1999 S4 (LINEAR; hereafter LS4) as seen after its breakup in 2000 July–August (Weaver et al. 2001). The morphology of both comets shows debris spread in a triangular structure spreading along the comet–Sun line.

Due to its proximity and breakup, the world-wide study of the comet 73P/2006 was extensive. *Chandra*'s contribution, discussed in this paper, is unique owing to its well-calibrated sensitivity to photons with energy above 300 eV, superior spatial resolution, and spectroscopic capability. Several other comets have now been studied with *Chandra* with which to compare our

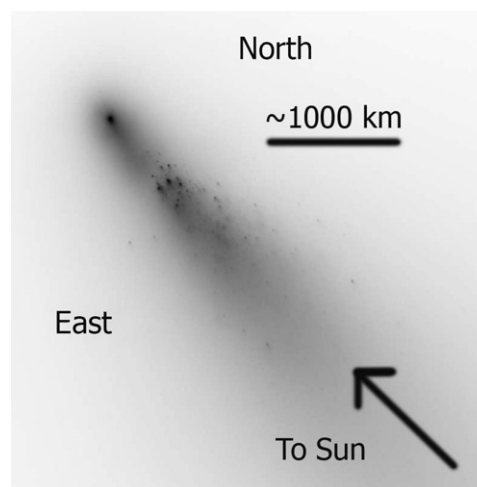


**Figure 1.** *HST* image of 73P/B from 2006 April 18 using F606W on the ACS/WFC. North is up and east is to the left. Multiple fragments trail the main fragment with the bulk of the comet–Sun line, which was nearly aligned with the cometary motion. Image by Weaver et al. (2006; <http://hubblesite.org/newscenter/archive/releases/2006/18/image/a/>).

results. In the case of SW3, *Chandra* observed the most variable large fragment, Fragment B (73P/B), from which over 35 other tracked fragments have been attributed, while *XMM-Newton*, *Swift*, and *Suzaku* observed Fragment C, most likely the parent nucleus of the active fragmentation.

This paper discusses the *Chandra* observations of 73P/B. There were several crucial aspects, which motivated this observation. First was the very close approach of the comet to the Earth. The nine comets observed with *Chandra* have ranged in spacecraft–comet distance from 0.26 AU (8P/Tuttle; 2008 January) to over 1.6 AU (Holmes; 2007 October) with a mean distance of 0.71 AU. At a distance of 0.1 AU, 73P/B held the possibility of unprecedented spatial resolution as well as a minimum of difference between the state of the solar wind as measured by near-Earth satellites and that experienced by the comet. Second was the expected low outgassing rate of the comet. This allowed for the possibility of identifying changes in the spectral signature across the coma. Spectral changes as a function of position were predicted by Bodewits et al. (2007), but have not been seen. Third, we hoped to better understand the disintegration process the comet was undergoing by investigating the interaction of the neutrals emanating from the comet with the solar wind.

In Section 2, we discuss the basics of the observations, including the solar wind data, the X-ray data, the basic X-ray morphology, and temporal variations. In Section 3, we discuss the spectral fitting using a charge-exchange (CXE) constrained model. We find that the CXE fit works, but that there is an anomaly at low energy introduced by lines that are below our fitting energy. We discuss the implications of our observations and model fits discussion in Section 4. We start by discussing the overall morphology, including density enhancements and gas production. In Section 4.3, we delve into the details revealed by the spectroscopy, including the state of the solar wind as ascertained from the X-ray data and the spectral structure of the comet. We close the discussion in Section 4.5 by comparing 73P/B with other comets observed in the X-ray, first by comparison of the X-ray to bolometric luminosities among several comets and then by comparing the X-ray observations of 73P/B to the previously unanalyzed postbreakup observations of Linear/S4. In Section 5, we summarize our conclusions.

<sup>8</sup> <http://ssd.jpl.nasa.gov/horizons.cgi>.

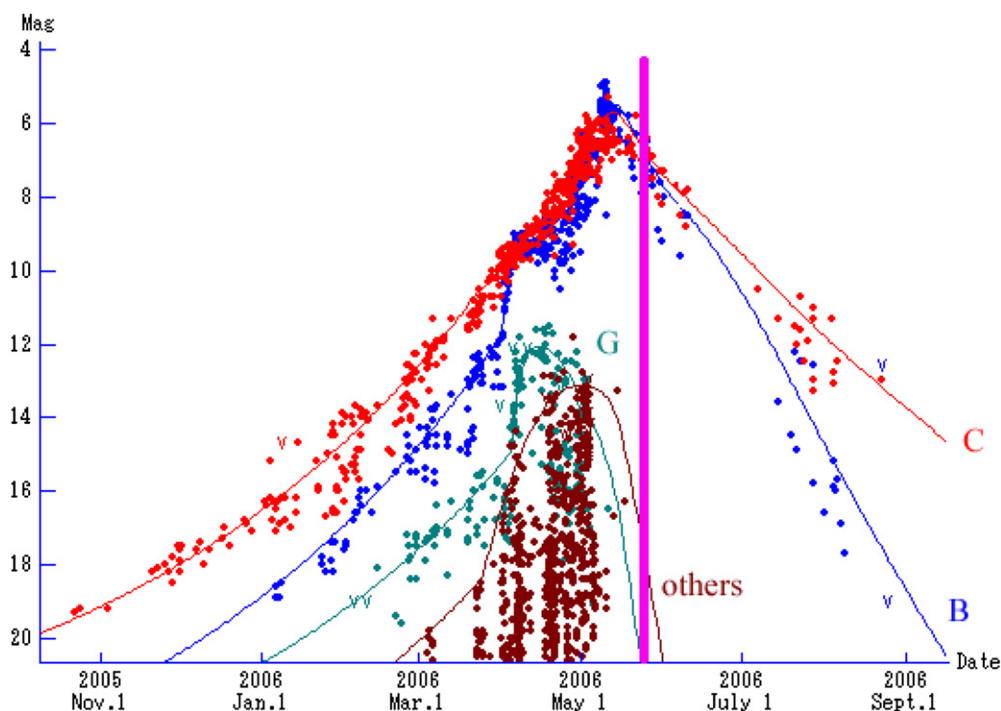


**Figure 2.** Light curve of various fragments of comet 73P/2006. Compiled by Yoshida (<http://www.aerith.net/comet/catalog/0073P/index.html>). Fragment B brightened suddenly in 2006 April and was as optically bright as the C Fragment at the time of the *Chandra* observation—indicated by the vertical line.

## 2. OBSERVATIONS

### 2.1. X-ray

*Chandra* observations of comet 73P/B were obtained on 2006 May 23 in 6 hr (20 ks), using the ACIS-S CCD spectral array, which combines the abilities to image X-rays at a platescale of  $0.5''/\text{pixel}$ , and to produce well-calibrated, moderate resolution spectra ( $\Delta E \sim 110$  eV FWHM,  $\Delta E_{\text{Gaussian}} = 49$  eV) from 0.30 to 2.0 keV. ACIS has six active CCDs. Each CCD as an  $8'$  field of view (FOV). The gap between the chips was  $22''$  in the horizontal direction and  $163''$  in the vertical direction. Our analysis, and the aimpoint of the telescope, focused on the back-illuminated S3 chip that has better low energy sensitivity than the other chips. During the *Chandra* observation, 73P/B was 0.97 AU from the Sun and 0.10 AU from the Earth, with a total visual magnitude of  $V \sim 7.5$  (Figure 2), a total luminosity of  $L_{\text{optical}} \sim 7.25 \times 10^{17}$  erg  $\text{s}^{-1}$ , and an estimated  $Q_{\text{gas}}$  of  $2 \times 10^{28}$  mol  $\text{s}^{-1}$  (Schleicher 2006) moderately active for an ecliptic comet.

We obtained five pointed *Chandra* observations of 73P/B on 2006 May 23 from 05:30 to 11:45 UT each of  $\sim 65$  minutes (3.7 ks). Data were taken in a “very-faint” (VF) mode with a 3.2 s frame time and an energy filter which excluded energies above 13 keV to prevent telemetry saturation. Standard processing applies a VF filter to exclude additional events that are generally not caused by X-rays. On downlink data with grade values of 1, 5, and 7 were excluded, as they are generally not X-rays.

The method of *Chandra* observation was kept simple: the ACIS-S array was pointed on the sky  $2'$  in front of the comet along the direction of its apparent motion, and the comet was allowed to move through the FOV. No active guiding on the comet was attempted. The predicted location of the B nucleus crossed the aimpoint  $2'$  from the northwestern edge of the S3 chip, 2 ks into each observation. Thus, the nucleus was only on the S3 CCD about 75% of the exposure. After 2 ks, the telescope

was repointed by about 8 arcminutes to the south–southwest and the process was repeated. Repointing took approximately 400 s. The direction to the Sun is  $21^\circ$  south of due west. Fragment C, which indicates the orbital direction of motion, is in the direction  $71^\circ$  south of west ( $dR.A. \cdot \cos \text{decl.}/dt = 357''.0 \text{ hr}^{-1}$ ,  $d(\text{decl.})/dt = -222''.1 \text{ hr}^{-1}$ ).

*Chandra* observations return a list of time-tagged detections of individual photon pulse heights and spatial locations. After removing three noted point sources, we constructed a comet image with the photons remapped into a coordinate system moving with the comet’s nucleus using the “sso\_freeze” algorithm, part of the *Chandra* Interactive Analysis of Observations (CIAO) software. The layout of the observations on the sky and reprojected into comet-centric coordinates is shown in Figure 3. The resulting effective FOV of the back-illuminated S3 chip in the comet-centric coordinate system was about  $10' \times 10'$ .

A total of 1865 photons were detected from the comet in the 300–1200 eV range in the central elliptical emission region. The average count rate in the 300–1200 eV energy range over 20.8 ks of observations was 0.13 cps, similar to the 0.1 cps rate found for comet Encke in 2003 (Lisse et al. 2005). Spectra were compared to a solar wind velocity sensitive CXE model (Bodewits et al. 2007) using the XSPEC fitting routines (Arnaud 1996). This model is discussed in more detail in Section 3.

### 2.2. Solar Wind

Because of its close approach to Earth—relative to other comets observed at X-ray wavelengths—comet 73P/B allowed us, for the first time, to link observed X-ray spectra from the coma with the directly measured physical conditions of the solar wind, which enter the interaction zone. We obtained solar wind data from the online data archives of *Advanced Composition Explorer* (ACE) (proton velocities and densities from the Solar Wind Electron, Proton, and Alpha Monitor (SWEPAM) instrument, heavy ion fluxes from the Solar Wind

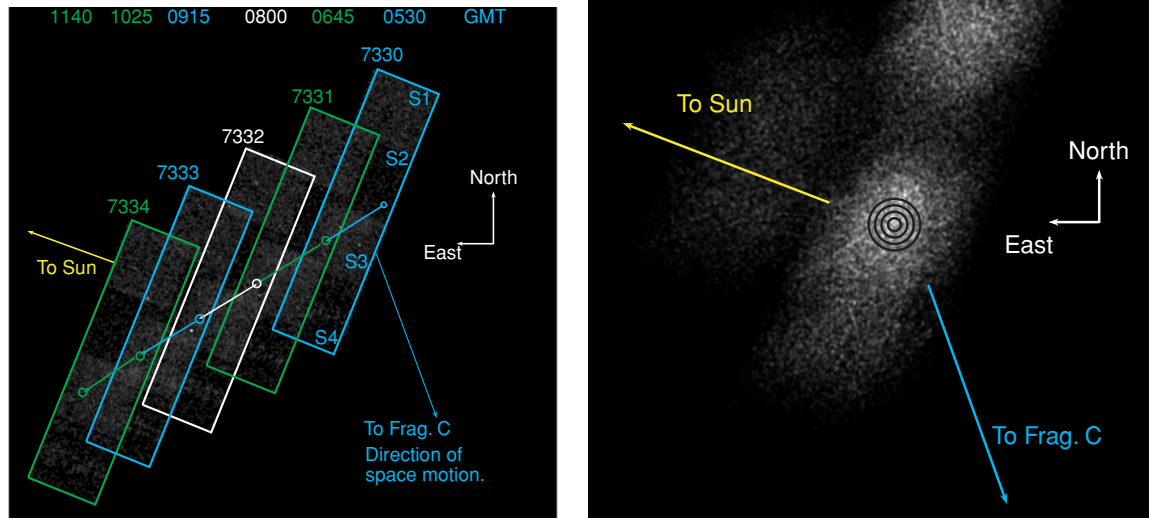


**Figure 3.** Layout for *Chandra* observations. Left: in the frame of the spacecraft. The S1–S4 chips are rendered from all five pointings (Obs ids 7330–7334). Chip IDs are noted in observation 7330. 73P/B tracks about  $140^\circ$  east of north. This is mostly reflex motion, the actual space motion of the comet toward Fragment C, about  $210^\circ$  east of north. The Sun is  $70^\circ$  east of north. The numbers along the top map to circles along the track and indicate the time the comet was at a particular position. All the times indicate the beginning of an observation—in UT 2006 May 23—except “1140,” which was the end of the last observation. Right: the same data, with chips I2 and I3 included and all data reprojected onto the comet’s frame of reference. The “bulls-eye” pattern indicates the location of the nucleus. The apparent signal in the S1 chip at the upper right is not due to X-ray emission from 73P/B. The diameter of the rings are  $1'–4'$  inclusive.

(A color version of this figure is available in the online journal.)

Ion Composition Spectrometer (SWICS) and Solar Wind Ion Mass Spectrometer (SWIMS) instruments<sup>9</sup>) and *Solar and Heliospheric Observatory* (*SOHO*) (proton fluxes from the Proton Monitor Instrument<sup>10</sup>). Both *ACE* and *SOHO* are located near Earth, at its Lagrangian point L1, at 0.01 AU from the Earth. In order to map the solar wind from L1 to the comet position, we used the time shift procedure described by Neugebauer et al. (2000). The calculations are based on the comet ephemeris, the location of L1, and the measured solar wind speed. With this procedure, the time delay between an element of the corotating solar wind arriving at L1 and the observed X-ray emission can be estimated. During our observations, solar wind observed at L1 arrived at the comet within less than 5 hr. For comets previously observed by *Chandra*, the typical delay was over 41 hr. The solar wind proton velocity and heavy ion composition around the observations are shown in Figure 4.

### 2.3. Morphology

At a distance of 0.1 AU, the resolution of *Chandra* equates to a spatial resolution of about 50 km per pixel. Since our X-ray observations were photon starved, smoothing is required to improve the signal-to-noise ratio (S/N). Overall there were about 1000 photons between 350 eV and 1.2 keV detected within  $100''$  of the nominal location of the comet nucleus. This is an area of about  $30,000''^2$  so only one photon was detected per box  $5''.5$  on a side. The background is about  $0.14 \text{ count s}^{-1}$  on the S3 chip.<sup>11</sup> To obtain  $3\sigma$  noise statistics, we require at least 10 counts  $\text{pixel}^{-1}$ . This provides an effective pixel of about  $18'' \times 18''$  (or a spatial resolution of about 1000 km).

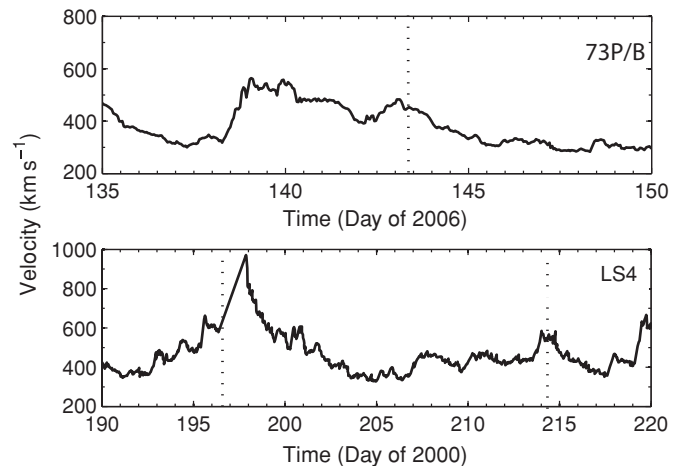


**Figure 4.** Solar wind proton velocities estimated from *SOHO* proton monitor data for 73P/B (top) and LS4 (bottom). The time of the observations is indicated with a dotted line. The data were mapped to the position of the comet using a radial and corotational extrapolation scheme.

The ACIS detector has two back-illuminated (S1 and S3) and four front illuminated (S2, S4, I0, I1) CCDs. The advantage of the back-illuminated CCDs is that they have greater sensitivity below 800 eV and thus are more sensitive to the dominant CXE lines at the expense of somewhat lower energy resolution. Chips S1 and S3 show the strongest apparent emission primarily due to their high sensitivity below 500 eV (Figure 3). However, the S1 background is known to be higher than S3 and these values are indicative of a somewhat larger excess on S3 because the background level of S1 is about 25% higher than S3 and we expect the background to be about 1000 counts higher on S1.<sup>12</sup>

<sup>9</sup> <http://www.srl.caltech.edu/ACE/ASC/level2/index.html>.

<sup>10</sup> <http://umtof.umd.edu/pm/crn/>.

<sup>11</sup> *Chandra* Proposers Observatory Guide (POG) Version 9.0 Section 6.15 Table 6.10.

<sup>12</sup> Same as footnote 11.

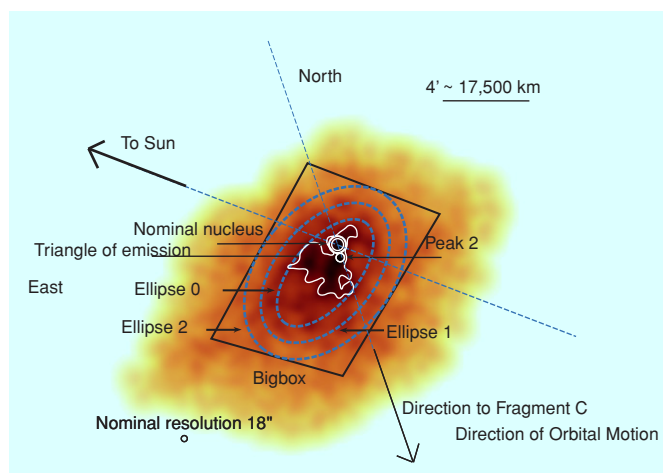


**Figure 5.** *Chandra* image of 73P/B. Data from CCD S3 are shown. Image has been scaled and stretched to highlight details. Red has been power law stretched to highlight bright, high spatial frequency (less than  $18''$ ) features. Green has a less extreme squared stretch to highlight moderate intensity, high spatial frequency features. Blue shows a linear stretch to show the extent of all X-rays. Colors are inverted to enhance contrast (for presentation purposes). Thus, high frequency intense features are black, moderate features are red to orange, and faint diffuse features are yellow. Regions of interest are identified, including the elliptical emission regions (blue dashed lines), the triangle of emission (solid white contour), various peaks within the triangle of emission including the nucleus (solid white circles). The effective point-spread function (PSF), critical vectors, and a length scale bar are also shown as additional regions used for spectral extraction and tabulated in Tables 2. Bigbox, Ellipse 0, and Circ100 refer to all data within the region. Ellipse 1 and Ellipse 2 are annular regions excluding all data outside of the  $50''$  wide ring. Likewise, Ellipse 0 with Circ100 excluded. The image is not corrected for exposure variations.

Concentrating on the morphology of the data on the S3 chip, we restrict the data to nominal energies below 1000 eV and above 300 eV, where the bulk of the detectable CXE lines has been found for other comets. To create a visualization which reflects the  $18''$  resolution, the data were smoothed to create an image using the CIAO tool *csmooth* to a resolution of about  $12'' \times 12''$ . A second version of the *csmooth* algorithm was run

at a resolution of about  $8'' \times 8''$ . A composite of these images is shown in Figure 5. The smoothed images show the primary emitting region to be about 25,000 km in extent in the Sunward direction and about 40,000 km in the orthogonal direction. The peak of the emission is not significantly displaced from the nominal B nuclear location. There is a second peak of about 90% the strength of the nucleus about  $50''$  to the southwest, or about 2.5 resolution elements off of the direction of motion, in the forward direction. The 73P/B emission is almost entirely contained on the S3 chip—there is no evidence of the CXE signal on the S2 and S4 chips (Table 1).

Overall, we identify five structures: (1) the background—essentially the corners of S3, (2) an outer ellipse with its minor axis oriented along the direction of motion, (3) a triangular polygon within the emitting region, (4) the nominal nuclear peak (which is *not* detected as an enhancement), and (5) a lesser peak displaced from the nominal nuclear peak by about  $50''$  in the direction of fragment “C.” To quantify the various structures, we calculated the counts in each region. The general emission is widely dispersed over about 50,000 km roughly east to west and roughly 75,000 km north to south. The brighter emission (triangle) is displaced north of the main emission but still south of the nucleus. In Table 1, we calculate the surface brightness in counts per pixel of each region and the brightness of each region above the overlaying region. From this table, it is clear that the oval region is a true region of excess emission above the background and that the triangle is clearly brighter than the ellipse. There is 98% confidence that the nuclear peak is real and about 85% confidence in peak 2. It is important to note that this sort of complicated X-ray structure has been observed for only one other comet to date, Linear/S4 (Lisse et al. 2001).

In the broadest energy range, 300–1200 eV, 73P/B appears roughly elliptical in shape, with the major axis aligned with the direction of apparent motion (see the left-hand side of Figure 3). Data in the softest bands, 350–500 eV, which should be dominated by emission from carbon and data in the middle band, 500–700 eV, which should be dominated by emission from ionic oxygen, show three concentrations of emission near the

**Table 1**  
Total Counts in Various Regions of 73P/B

Location	Area (pixels)	Counts <sup>a</sup> (net)	Surface Brightness (counts pixel <sup>-1</sup> ) <sup>b</sup>	Error Surface Brightness (counts pixel <sup>-1</sup> ) <sup>c</sup>	Sigmatas above Background
All events on I2	1048580	1148	1.09	3.23	...
All events on I3	1048580	1005	0.96	3.02	...
All events on S1	1048580	6115	5.90	7.45	...
All events on S2	1048580	1472	1.40	3.65	...
All events on S3	1048580	6183	5.89	7.50	...
All events on S4	1048580	1598	1.52	3.81	...
Background (on S3)	384845	1121	2.91	9.18	...
Bigbox	922907	4673	5.06	7.41	29
Ellipse 0	256072	1702	6.65	16.11	23
Ellipse 1 (–E0)	210801	1149	5.45	16.08	16
Ellipse 2 (–E1)	273633	990	3.62	11.50	6
Triangle	64335.7	783	12.17	43.49	20
Nucleus (circ100)	31415.9	279	8.88	53.16	...
Peak 2	2259.8	30	13.2	242.24	<3 <sup>d</sup>

**Notes.**

<sup>a</sup> Energy range is 0.3–1.0 keV.

<sup>b</sup>  $\times 10^{-3}$ .

<sup>c</sup>  $\times 10^{-5}$ .

<sup>d</sup> Above the “triangle.”

nucleus. A central concentration of flux is associated with the nuclear peak and peak 2; there is another concentration of flux to the south along the southern edge of the triangle and a third concentration near the northern apex of the triangle. Harder channels show a strong peak at the southwestern apex of the triangle, with little additional coherent emission. An interesting preliminary result is the relatively limited area of overlap among the emission regions when photons are sorted by energy. This indicates that the oxygen emission arises from different regions than the carbon emission.

Since the morphology driven by the dynamical behavior of solid material emitted from a comet's nucleus, we need to consider the modifying effects of solar radiation. We ignore the effects of the solar wind (charged particle energy deposition, spallation, charging, and E-M forces from the fields embedded in the wind), as these are negligible for particles of radii greater than  $0.1 \mu\text{m}$  (Burns et al. 1979; Horanyi & Mendis 1986, 1991). Solar gravity treats the emitted dust the same way it treats the comet's nucleus, that is, the dust tracks the comet's Keplerian orbit (with typical heliocentric velocities of  $10\text{--}50 \text{ km s}^{-1}$ ), modulo the minor perturbation from the terminal velocity ( $0.001\text{--}0.5 \text{ km s}^{-1}$ ) imparted by the emission process and expanding coma gases (Lisse et al. 1998, 2004). Solar radiation pressure shows its effect as acceleration in the antisolar direction (an outgassed particle effectively sees a lower mass sun than does the nucleus), affecting all particles, proportional to the product of the surface area multiplied by the photon absorption-scattering efficiency/mass. The most pronounced effect is on small particles with a size of  $\sim 1.0 \mu\text{m}$  with high surface area/mass ratios and high resonant scattering efficiency for the optical photons that dominate the Sun's spectrum by number.

For small particles, the parameter  $\beta \sim 0.47/(\rho \times a (\mu\text{m}))$  is used to evaluate whether the effect of gravity or wind pressure will dominate the trajectory of a particle. The limiting cases help us bound the range of dust particles' dynamical behavior. When  $\beta \sim 1$ , the forces on dust are large enough that it moves down and out of the comet's tail within hours to days. For the  $\beta > 1$  ( $\sim 0.1\text{--}1 \mu\text{m}$  radius) particles, the net acceleration is so large that the antisolar direction is approximately constant over the few days that the dust is present in the tail, and the dust trajectory is roughly linear in the antisolar direction (see the antisolar structure evident in the *HST* images of 73P/B, Figure 1, and in the multiple tail structures of the *Spitzer*  $24 \mu\text{m}$  image of the fragment train of Reach et al.<sup>13</sup>). For  $\beta < 0.001$  (radius greater than  $500 \mu\text{m}$ ), the net acceleration in the comet frame is very small, the particle remains in the vicinity of the nucleus for many months, and the particles slowly spread out along the comet's velocity direction due to the Keplerian shear imparted by the velocity of expulsion (see the line of emission from large dust lying along the comet's orbital path and "connecting" the individual fragments in the *Spitzer*  $24 \mu\text{m}$  mosaic of Reach et al.<sup>14</sup>). The abundant intermediate sized particles with  $1 > \beta > 0.001$  ( $1\text{--}500 \mu\text{m}$  radius), which contain much of the emitted mass from 73P/B, follow trajectories between these two extremes (see Figure 6 of Reach et al. 2000, 2007). We thus expect to find them, and any gas emitted by them, to lie in a spatial region between the antisolar direction vector and trailing direction of the comet's motion. This interpretation is complicated by the CXE mechanism that emits a photon for each interaction with a released neutral. Once released, the neutrals travel in random directions and have been

seen to persist over  $100,000 \text{ km}$  away from their source (see Tempel 1—Lisse et al. 2007). Hence the emission should, and does, fill the field. Any signature of multiple emitting sources would have to be seen above this overall signal. While the signal to noise in Figure 5 cannot support this interpretation, the bulk of the flux is seen either coincident with the nucleus or in the direction toward the Sun, relative to the nominal nuclear position.

#### 2.4. Temporal Variation

Temporal variation has been previously studied in several comets. Impulsive events were seen in several X-ray observations of comets (Lisse et al. 1996, 1999, 2001—Hyakutake, Encke, and Linear S4 respectively). X-ray observations of the 2003 passage of Encke (Lisse et al. 2005) indicated a  $\sim 11.1 \text{ hr}$  periodicity attributed to nuclear rotation. Observations of Tempel 1 associated with Deep Impact (Lisse et al. 2007) showed not only the flare associated with the impact, but also a quasi-periodic brightening with a two-week period. For 73P/B, temporal variability could also provide another line of evidence about the reality of the features. We examined four time slices of the data, each covering about  $5000 \text{ s}$ . Conclusions from these time slices include the following.

1. The nuclear region is always bright.
2. Peak 2 is always brighter than the surrounding material.

We studied flux changes to look for variations on shorter timescales. The mean count rate in the central "triangle" region was about  $9.0 \pm 3.0$  counts per  $200 \text{ s}$ . Of the samples unaffected by repointing, one was high by (almost exactly)  $3\sigma$  from the mean flux rate. Another sample was remarkably low by  $2.7\sigma$ . Neither deviation was adjacent to a second deviation of similar magnitude. Hence, there is no evidence of temporal fluctuations of the X-ray flux larger than  $10\%$  during the  $6 \text{ hr}$  period of observations.

### 3. SPECTRAL FITTING AND RESULTS

We extracted spectra from several regions centered on the comet with a minor axis along the comet–Sun line in the S3 chip, and from several apertures on the adjacent S2 and S4 chips. The apertures for the S3 chip included (1) a large box-shaped aperture to include as many counts as possible for a total, high signal-to-noise spectrum (bigbox), (2) approximately annular ellipse at increasing larger radii from the nucleus to find any changes in the spectrum (these are called Ellipse 0, Ellipse 1, and Ellipse 2—see Figure 5), and (3) the triangular region mentioned in Section 2.3 (morphology). We do not individually examine the pointlike peaks due to their low intrinsic brightness.

The spectra were extracted using the standard CIAO (v3.4) tools, including the creation of the Ancillary Response Function and Redistribution Matrix Function files that compensate for local and temporal variations in the ACIS response. While the regions are extracted in the comet's frame of reference, the analysis is done in fixed chip coordinates so that appropriate responses are used. Background spectra were extracted from comet emission-free regions from the anti-Sun side of the S3 chip.

The data were fitted to the CXE model as presented in Bodewits et al. (2007). In this CXE model, each group of ions in a species was fixed according to its velocity-dependent emission cross sections to the ion with the highest cross section in that group. Thus, the free parameters were the relative strengths of H- and He-like carbon ( $299$  and  $367 \text{ eV}$ ), nitrogen (N v at

<sup>13</sup> <http://www.spitzer.caltech.edu/Media/releases/ssc2006-13/index.shtml>.

<sup>14</sup> Same as footnote 13.

**Table 2**  
Results of the  $v = 450 \text{ km s}^{-1}$  CXE Model Fit for the 73P/B Spectra Sorted by a Spatially Selected Region

Energy	Circ100	EllInner <sup>a</sup>	Ellipse 0	Ellipse 1	Ellipse 2	Bigbox	Triangle	LS4 (part2)
653 (O VIII)	<0.1 <sup>b</sup>	0.7 ± 0.2	1.4 ± 0.4	1.2 ± 0.3	1.3 ± 0.3	3.4 ± 0.9	0.6 ± 0.2	10.1 ± 1.2
561 (O VII)	1.3 ± 0.3	3.6 ± 0.8	7.1 ± 1.0	4.4 ± 0.6	4.3 ± 0.6	14.9 ± 1.2	3.2 ± 0.6	8.4 ± 1.6
367 (C VI)	<2	<13	11.9 ± 7.0	9.6 ± 5.4	7.5 ± 5.4	<25	<6	33 ± 8
299 (C V)	57.3 ± 16.4	134 ± 63	234 ± 72	140 ± 61	102 ± 52	518 ± 169	112 ± 35	65 ± 33
500 (N VII)	<0.6	<1.1	<1.5	<0.8	<0.7	<2	<1.0	<4
419 (N VI)	1.4 ± 0.8	<5	9.2 ± 4.3	5.2 ± 3.2	<4	19.5 ± 8.9	6.5 ± 2.3	<8
907 (Ne VIII)	<0.1	0.3 ± 0.1	0.5 ± 0.1	0.4 ± 0.1	0.3 ± 0.1	1.1 ± 0.5	<0.1	5.6 ± 0.9
1023 (Ne IX)	<0.1	<0.1	0.3 ± 0.2	0.3 ± 0.1	0.4 ± 0.2	1.3 ± 0.6	0.2 ± 0.1	5.6 ± 1.1
$\chi^2$	52.1	56.3	61.4	38.2	40.5	41.0	46.4	96.8
$\chi^2/\text{dof}$	1.27	1.37	1.50	0.95	1.04	1.0	1.13	2.36
Log model flux	-13.21	-12.63	-12.37	-12.56	-12.65	-12.10	-12.73	-12.14
Line ratios								
653/561	0.0	0.18 ± 0.07	0.19 ± 0.06	0.26 ± 0.07	0.30 ± 0.08	0.23 ± 0.06	0.20 ± 0.08	1.20 ± 0.27
367/299	0.01	0.06	0.05 ± 0.03	0.07 ± 0.05	0.07 ± 0.06	0.03	0.02	0.52 ± 0.26
299/561	16.3 ± 6.0	37.4 ± 19.4	33.0 ± 11.1	32.1 ± 14.7	23.9 ± 12.6	34.7 ± 11.7	35.2 ± 12.8	7.7 ± 4.2

**Notes.** Fluxes are given in units of  $\text{erg cm}^{-2} \text{ s}^{-1}$ . Errors are obtained by averaging over the calculated  $\pm 90\%$  confidence contours (corresponding to  $\chi^2 = 2.7$  or  $1.6\sigma$ ).

<sup>a</sup> Ellipse 0 with “Circ100” emission subtracted.

<sup>b</sup> “<” denotes a 90% confidence upper limit.

419 and N VI at 500 eV), and oxygen (O VII at 561 and O VIII at 653 eV). Additional Ne lines, the Ne IX forbidden, intercombination and resonance lines around 907 eV and the Ne x Ly $\alpha$  at 1023 eV were also included in our CXE model, giving a total of eight free parameters. Spectral parameters were derived using the least-squares fitting technique with the FTOOLS XSPEC package (Arnaud 1996).

In the model, the lines were assumed to be intrinsically sharp, only broadened by the instrumental resolution ( $\sim 50$  eV). The spectra were fitted in the 300–1000 eV range. This provided 49 spectral channels, and thus 41 degrees of freedom (dof). Difficulties in modeling ACIS spectra below 300 eV have already been discussed in Lisse et al. (2001, 2007), as a result of the rising background contributions and decreased effective area near the instrument’s carbon edge. Thus, fitting below 300 eV was not attempted here.

A sample spectrum fitted with the full CXE model is shown in Figure 6. We show the spectrum of the largest aperture centered on the S3 chip and the residuals to the fit and input CXE model. This spectrum showed strong emission lines of C V (299 eV), C VI (367 eV), N VI (419 eV), and O VII (561 eV) as seen in previous comets (Lisse et al. 2001, 2005, 2007; Krasnopolsky et al. 2002; Bodewits et al. 2007). N VII at 500 eV was not significant and there were 1–3 $\sigma$  detections of Ne VIII (907 eV) and Ne IX (1023 eV) lines. Spectral fitting results for the full CXE model with a solar wind velocity  $v = 450 \text{ km s}^{-1}$  are summarized in Table 2. Fluxes are given in units of  $\text{erg cm}^{-2} \text{ s}^{-1}$ . Errors are obtained by averaging over the calculated  $\pm 90\%$  confidence contours (corresponding to  $\chi^2 = 2.7$  or  $1.6\sigma$ ). Goodness of fit parameters, fluxes, and the most significant line ratios are also listed. The overall X-ray flux from the comet was  $8.0 \times 10^{-13} \text{ ergs cm}^{-2} \text{ s}^{-1}$ , corresponding to a total X-ray luminosity from 0.3 to 1.0 keV of  $2.3 \times 10^{13} \text{ ergs s}^{-1}$ . About 25% of the flux comes from a small triangular region located forward of the nucleus relative to the direction of motion.

The columns of Table 2 are arranged spatially. The first fit is for a small circle 100 pixels in diameter centered on the nominal nucleus. The next three fits are cylindrical shells of an elliptical cross section moving progressively outward. The final column lists fitting results to the C/1999 S4 (LINEAR,

hereafter LS4) postbreakup spectra (extracted for the same large square “bigbox” region as 73P/B), which we will compare to our 73P/B results in Section 5.

We have searched for changes in the spectra as a function of distance from the nucleus. In Figure 7, we compare spectra from the inner region and the very central 100 pixels centered on the nominal nucleus. The spectra are scaled by the area of each region and show more relative total counts in the inner region. The innermost spectrum shows very weak emission with O VII being the most significant. Spectra from further away from the nucleus show an increased amount of oxygen emission, with the O VII emission increasing a factor of 4–5 and the O VIII emission doubling from the middle to outer region.

Figure 8 compares outer, middle, and inner ellipse spectra in the 300–1000 eV range. The relative strengthening of the carbon feature is clearly visible. We discuss the ion line ratios as a function of distance from the nucleus and CXE cross sections in Section 4.2.

#### 4. INTERPRETATION AND DISCUSSION

73P/B is (or perhaps was) a unique object for study in three critical ways. First, it passed very close to the Earth, presenting us with an unequalled opportunity to study the morphology at high spatial resolution. Second, it was a weakly outgassing object, possessing a collisionally thin (to CXE) coma, allowing us to test CXE physics in a collisionally thin medium. Finally, it fragmented as we observed it, allowing additional insight into the evolution of comets. Its X-ray morphology (see Figure 4 and Section 2.3) clearly differs from other comets observed by *Chandra* in that it lacks either the pronounced umbrella shape of the strongly outgassing comets (Hyakutake (Lisse et al. 1996), prebreakup SL4 (Lisse et al. 2001), McNaught-Hartley (C/1999 T1; Krasnopolsky et al. 2002), or Ikeya-Zhang (153P/2002; K. Dennerl et al. 2009, in preparation)) or the “strong point source with faint diffusive halo of emission” (Encke (2P/2003; Lisse et al. 2005); Neat (C/2001 Q4; Sasseen et al. 2006); Tempel 1 (9P/2005; Lisse et al. 2007)). Here we find that the key reason for the differences seen between 73P/B and other comets was the fragmentation process, releasing and diffusing solids that spread out extensively and *then* sublimated.

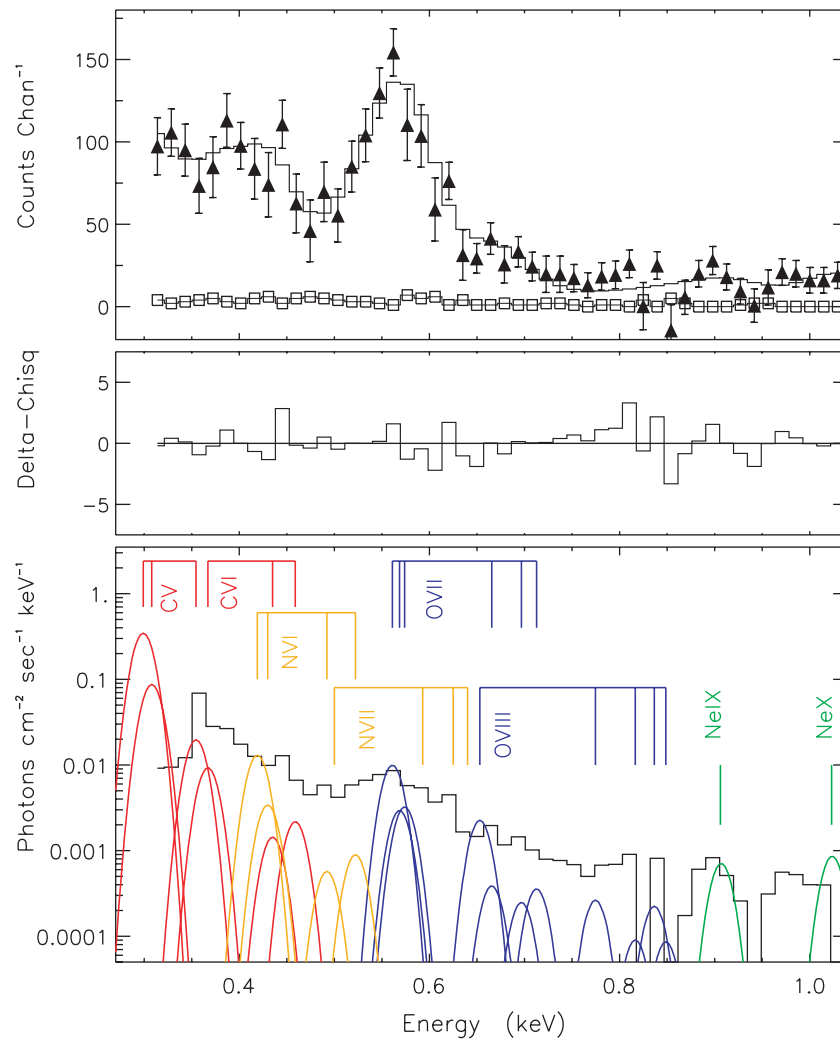


**Figure 6.** Details of the CXE model fit for the spectrum of comet 73P/B for the whole “bigbox” region. Top panel: the 73P/B count rate spectrum (filled triangles), a sample background (open squares), and best fit spectrum with the CXE model (solid histogram). Middle panel: residuals of the CXE fit ( $\chi^2/\text{dof} = 1.0$ ). Bottom panel: CXE model and observed spectrum indicating the different lines in the fit and their strengths. Carbon—red, nitrogen—orange, oxygen—blue, neon—green. The unfolded model is scaled above the emission lines for the ease of presentation. The apparently very strong C v line at 300 eV is enhanced due to contributions from lines at 250–300 eV.

#### 4.1. Morphology

The X-ray morphology of 73P/B is complicated by the nonuniform exposure due to the stare and shift observing approach on a moving solar system object. For this work, we have utilized a new capability in CIAO 4 to create an exposure map-corrected X-ray image of 73P/B.

The detail of this is shown in Figure 9. While the triangle of emission is still a clear feature in the exposure-corrected map, the strongest emission is toward its northern vertex. The bulk of the emission comes from roughly five regions of similar flux located either side of the comet–Sun line. The situation is further complicated by the ongoing disintegration of the comet. This means that nongravitational forces have a pronounced effect on the position of the B-fragment main mass. This may be the reason why the brightest region is not exactly at the aimpoint, but displaced by about  $12''$ .

It is relatively straightforward to understand why the three brightness centers lie along the orbital velocity direction. This emission comes from gas sublimating from large chunks of cometary material, at least 0.1 km effective radius or larger, released at small relative velocities in the recent past. For such

bodies, nongravitational forces such as asymmetric sublimation and radiation pressure are either insignificant or have not had enough time to act appreciably. Similar to the larger chain of  $\sim 50$  fragments observed (C-B-G etc.; see Reach et al. 2006), these chunks spread out slowly along the orbital direction of motion of the comet due to Keplerian shear (i.e., the small differences, on the order of one part in  $10^3$ , of their heliocentric velocities).

It is more difficult to understand why the extended diffuse emission appears to be in the Sunward direction. If the extended gas was coming from many icy fragments in a debris field, as suggested by *HST* observations of the 73P/B tail in 2006 April (Weaver et al. 2006), then these should be swept in the antisolar and antiorbital velocity directions from the chunks (see Lisse et al. 1998). The debris seen in the 73P/B *HST* time-lapsed imagery clearly moves away from the Sun and away from the direction of motion of the 73P/2006 large fragments (see Figure 1). If particles were the source of the CXE emission, the triangle of emission would be rotated by about  $45^\circ$  so that one side would be along the comet–Sun line away from the nucleus relative to the Sun. We can also rule out X-ray emission from small icy dust particles, on the order of 0.1–10  $\mu\text{m}$  in

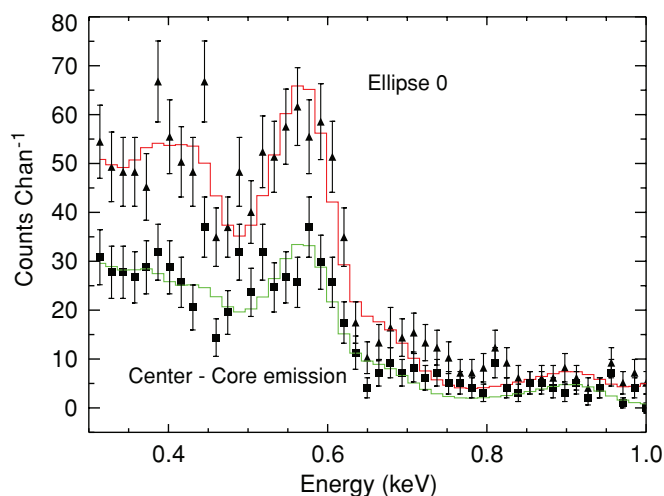


**Figure 7.** Comparison of the spectra near the comet's nucleus. We compare the central elliptical region (Ellipse 0) to the  $R = 100$  pixel circle (dubbed "center-core") centered on the nominal nucleus. Data within each region are fitted by a CXE model with a solar wind velocity of  $450 \text{ km s}^{-1}$  and highly ionized species of oxygen, carbon, nitrogen, and neon.

(A color version of this figure is available in the online journal.)

size, releasing appreciable amounts of neutral water gas as they are accelerated down the comet's tail by radiation pressure. Interestingly, the postdisintegration data from comet Linear S4 do show this pattern (see Section 4.5).

What is seen instead is emission in the solar direction, following along the chain of debris marked by the three brightness centers. One possible explanation for this is being due to overlapping emission from collisionally thin comae centered on each of the chunks, like several small comets strung out along a line. The emission of neutral gas (mainly water) is preferentially toward the Sun, because the Sun warms up this part of the comet the most.

#### 4.2. Estimating the Neutral Coma Gas Production

The X-ray emission of comet 73P/B can be used to make an estimate of the comet's bulk gas production rate. In the case of 9P/Tempel 1 after the Deep Impact experiment of 2005 July 4, an extension was seen in the *Chandra* images, identified with the icy material excavated from the comet by the impact (Lisse et al. 2007). The statistical significance of the extension was  $\sim 5\sigma$  above background. Larger scale imaging by the *Rosetta* spacecraft over the course of the next few days confirmed the progression of the water gas and OH ejected by the impact (Küppers et al. 2005). The estimated propagation velocity of the extension was  $0.5\text{--}1 \text{ km s}^{-1}$ . We use the estimated total mass of water ejected by Deep Impact ( $\sim 5 \times 10^6 \text{ kg}$ ) and the total on-target time of observation for Tempel 1 on July 4–5 of 130 ks to estimate the limiting sensitivity of *Chandra* to cometary activity as  $5 \times 10^6 \text{ kg}/130 \text{ ks}$  ( $5\sigma$ , equivalent to  $\sim 10^{26} \text{ mol s}^{-1}$  of  $\text{H}_2\text{O}$  at 1.5 AU). This sets the lower limit on the observed neutral ( $\text{H}_2\text{O}$ , CO,  $\text{CO}_2$  plus minor constituents) outgassing rate from 73P/B for the same solar wind conditions.

We can estimate a straightforward outgassing rate since the nominal detection of 73P/B was about  $25\sigma$  (Table 1). The observed outgassing rate is  $\sim 3 \times 10^{27} \text{ molecule s}^{-1}$  ( $\pm 50\%$ ). This is consistent with the 73P/B water production rate values of  $1.0 \pm 0.2 \times 10^{27}$  and  $7.2 \times 10^{27}$  measured about 1 month before the *Chandra* observation (Villanueva et al. 2006; Schleicher 2006, respectively). On the other hand, it is less than the

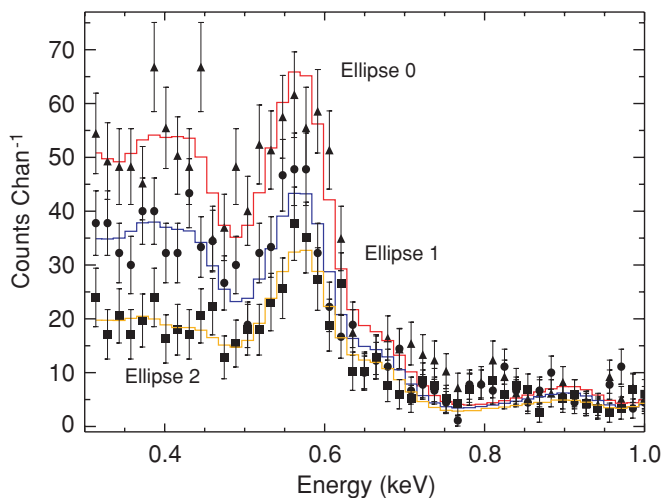


**Figure 8.** Comparison of count rate spectra for the larger scale structure of the comet. We compare the three elliptical annular apertures with a semimajor axis of 380, 480, and 580 pixels for Ellipse 0, Ellipse 1, and Ellipse 2 respectively. Spectra are fitted by the CXE model with a solar wind velocity of  $450 \text{ km s}^{-1}$ . All spectra show relatively strong emission from O VII and the innermost regions show the strongest C VI and C V emissions.

(A color version of this figure is available in the online journal.)

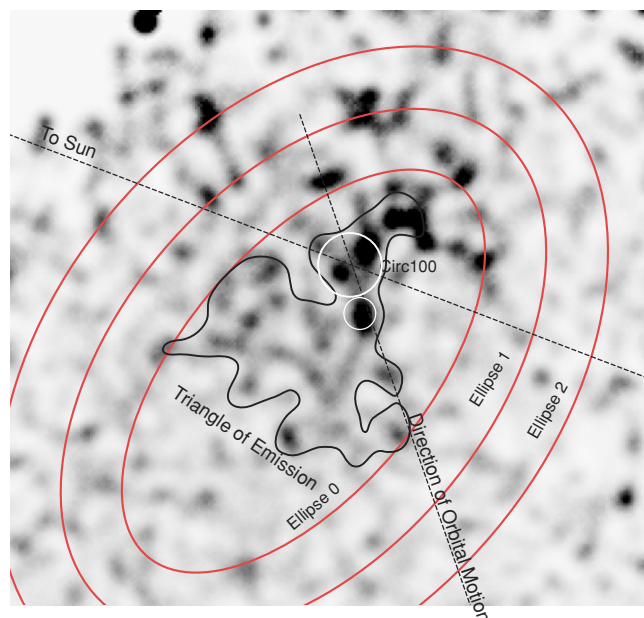


**Figure 9.** Detail of the central  $\sim 20,000 \text{ km}$  of the ACIS field. These data have been flux corrected by the exposure time and smoothed to about  $18''$ . A similar markup to Figure 5 is used. The extreme stretch of this image makes global details less apparent than Figure 5. The triangle of emission is less pronounced than in the nonflux-corrected image but still present.

(A color version of this figure is available in the online journal.)

$2 \times 10^{28} \text{ mol s}^{-1}$  ( $\pm 30\%$ ) measured by D. Schleicher (2006, private communication) using narrowband optical photometry on 2006 May 17–18. Bonev (2008) measured  $Q = 1.75 \times 10^{28} \text{ molecules s}^{-1}$  on May 10. Schleicher also reported the water production rate decreasing by 25% between the two nights. This makes  $10^{28} \text{ mol s}^{-1}$  an upper limit as the activity level on the comet decreases monotonically from May 18 to May 23. The FOV used to determine the water production rate of Villanueva et al. (2006) is small, on the order of a few arcsec in radius, while that of Schleicher et al. is on the order of  $30''\text{--}1'$ . The FOV is important because this is not a comet that produces gas only at the nucleus, but is rather more extended due to

the ongoing breakup. Hence, we expect to have much larger water production estimates from the Schleicher e group, and these estimates are on roughly the same spatial scales (a few arcminutes) as determined from the analysis of the *Chandra* images.

There were some differences in the observing conditions between Tempel 1 and 73P/B. The most significant were the solar wind proton density and ionization state. The solar wind speeds experienced by Tempel 1 over the course of 2005 June 30–July 14 varied between 400 and 600 km s<sup>-1</sup>, with a median very close to the 450 km s<sup>-1</sup> value of the solar wind during the relatively brief 73P/B observation. The proton density for the week of the 73P/B observation of about three protons cm<sup>-3</sup> was lower than the mean density of eight protons cm<sup>-3</sup> seen the week of the Tempel 1—Deep Impact observation, even though the proton rate was varying by a factor of 2 during the Tempel 1 observation. The composition and ionization state of the solar wind were also somewhat different for observations of the two comets. During the observations of 73P/B, the O<sup>8+</sup>/O<sup>7+</sup> ratio was about half of that of the wind during the Tempel 1 observations. As we will demonstrate in the following sections, the ionization state of the solar wind can significantly affect the overall X-ray luminosity. Still, the inferred outgassing rate is very modest for a comet. It signifies a low activity comet or possibly a very small, active one.

### 4.3. Spectroscopy

#### 4.3.1. Spectral Classification of the Wind State

A survey of cometary spectra obtained with *Chandra* (Bodewits et al. 2007) suggested a classification based upon three competing emission features, that is, the combined carbon and nitrogen emission (below 500 eV), O VII emission around 565 eV, and O VIII emission at 653 eV. First, the low energy emission (less than 500 eV) seems to be anticorrelated with the oxygen emission. This can be explained in terms of the freezing-in temperature of solar wind ions; the charge state distribution of the solar wind reflects the temperature of its coronal source region. Colder source regions hence result in lower charge states. For carbon, lower freeze-in temperatures imply that more ions are in the He-like state (as opposed to a H-like state). At these low temperatures, most oxygen ions will be in the O<sup>6+</sup> state, which does not yield any X-ray emission detectable with *Chandra* via CXE, but UV photons instead. As a net effect, the emission shifts toward the softer part of the X-ray spectrum. This can be seen very clearly in the spectra of 73P/B and 2P/2003 (Encke). In the spectra of these two comets, the carbon/nitrogen features are roughly as strong as the O VII emission, as opposed to an X-ray spectrum arising from a comet interacting with a hotter heliospheric wind environment, such as the July 14 (day 196) observations of comet LS4 (see Figure 4). Examining space-borne solar wind data confirms that 73P/B indeed interacted with a “cold” wind. Around the time of the *Chandra* observations, a sequence of three high speed coronal hole streams passed the comet. Coronal holes allow escape from Sun to the solar wind of cold (~10<sup>6</sup> K) plasma from low in the corona, near the photosphere, as opposed to the usual outflow of hotter plasma (~2 × 10<sup>6</sup> K) from the top of the corona.

The ratio of O<sup>7+</sup> to O<sup>6+</sup> ionic abundances has been demonstrated to be a good probe of solar wind states. Zurbuchen et al. (2002) observed that the slow, warm wind associated with streamers typically lies within 0.1 < O<sup>7+</sup>/O<sup>6+</sup> < 1.0, corresponding to freezing in temperatures of 1.3–2.1 MK. In Figure 10, we

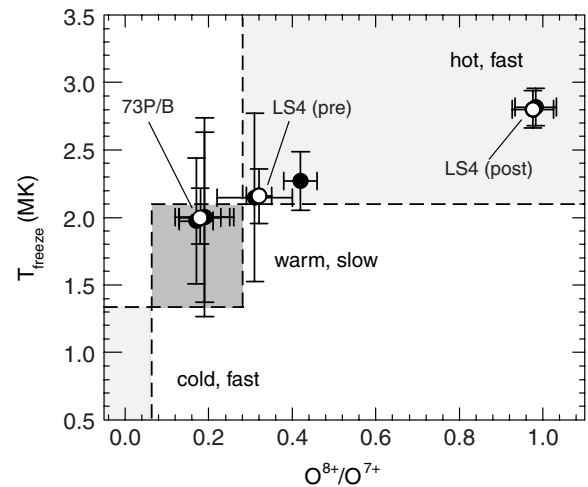


**Figure 10.** Spectrum-derived ionic oxygen ratios and corresponding freezing in temperatures from Mazzotta et al. (1998). Dots with error bars indicate all comets observed with *Chandra*. 73P/B and LS4 (pre- and postbreakup) are identified explicitly. LS4 postbreakup is nearly coincident with 153P/Ikeya-Zhang. The shaded area indicates the typical range of the slow solar wind (figure adapted from Bodewits et al. 2007).

show the observed O<sup>8+</sup> to O<sup>7+</sup> ratios and the corresponding freezing-in temperatures from the ionizational/recombination equilibrium model by Mazzotta et al. (1998). Most X-ray comet observations are within or near to the streamer-associated range of oxygen freezing in temperatures. The X-ray spectrum from 73P/B is consistent with its being in the warm, slow wind. This contradicts the fact that the space-borne data indicate a “cold” wind. Hence we believe the comet interacted with a corotating interaction region (CIR), a faster stream plowing through the background solar wind. It is a mixed state, in contrast to the “pure” cold polar wind, with which it might have interacted and which would have no O<sup>8+</sup> at all (Schwadron & Cravens 2000; Kharchenko & Dalgarno 2001).

#### 4.3.2. Solar Wind Abundances and Low Energy Contamination

The main advantage of 73P/B over previous comets observed in the X-ray regime was that it came so close that (nearly) in situ measurements of the solar wind were possible, enabling us to perform a direct test of our spectral modeling. Following the procedure laid out in Bodewits et al. (2007), the intensities of the spectral fit can be used to derive spectral abundances by weighting them with the relevant emission cross section. These results can then be compared with ionic abundance data obtained by the ACE/SWICS instrument. Averaging over the time of the observations, ACE/SWICS measured relative abundances of C<sup>5+</sup>/O<sup>7+</sup> = 7.6 ± 3.2 and C<sup>6+</sup>/O<sup>7+</sup> = 2.1 ± 0.7. (ACE data on the abundance of O<sup>8+</sup> and the nitrogen ions were not available during the time of the observations.) From the observations (Table 3), we derived relative abundance C<sup>6+</sup>/O<sup>7+</sup> = 2.1 ± 1. This result of the spectral analysis is in excellent agreement with the ACE measurements.

The obtained relative abundance we derive for C<sup>5+</sup> from the spectral analysis, however, is off by an order of magnitude—C<sup>5+</sup>/O<sup>7+</sup> = 87 ± 29. There are several factors that could account for this. The first possibility is an error in the ionic cross sections. Recent lab experiments suggest that at velocities around 450 km s<sup>-1</sup>, the theoretical emission cross sections for collisions with atomic hydrogen are about a factor of 2 smaller than measured emission cross sections for collisions between C<sup>5+</sup> and H<sub>2</sub>O molecules (Bodewits et al. 2007b).

**Table 3**Solar Wind Abundances Relative to  $O^{7+}$ , Obtained from the CXE-Model Fit

Ion	73P/B	LS4 (Postbreakup)
$O^{8+}$	$0.18 \pm 0.05$	$0.95 \pm 0.21$
$C^{6+}$	$<2.09$	$4.89 \pm 1.51$
$C^{5+}$	$87 \pm 29$	$19 \pm 10$
$N^{5+}$	$<0.10$	$<0.37$
$N^{6+}$	$1.76 \pm 0.82$	$<1.28$
$Ne^{10+}$	$0.04 \pm 0.02$	$0.33 \pm 0.09$

Second, while calibration errors for *Chandra* at 300 eV are relatively high, cross calibration with *XMM-Newton* indicates that these are much less than 50%. The quoted error for the absolute effective area of ACIS “ $<5\%$ .”<sup>15</sup> In addition, we see that this has been a persistent effect. Bodewits et al. (2007) used  $O^{8+}/O^{7+}$  versus ionization freeze-in temperature as a measure for the state of the wind. They showed that the correlation between ionization freeze-in temperature and  $C^{6+}/C^{5+}$  is poorly correlated, ostensibly because  $C^{5+}$  abundances are consistently too large. In the case of 17P/Holmes, D. Christian et al. (2009, in preparation) noted a similar issue.

It is therefore very likely that the  $C^{5+}$  emission feature is strongly contaminated by emission from several ions of species such as Mg, Si, Ne, etc. (Sasseen et al. 2006). The source of the discrepancy is probably related to the energy of the  $C^{5+}$  emission line and other low charge state ions, which lie just below 300 eV. These lines may be more important in 73P/B than in other comets if the charge state of the solar wind is relatively low. The flux is computed from the theoretical spectrum assuming no contribution from lines below 300 eV. Based on the *ACE* data, we estimate that as much of 90% of the emission around 300 eV should be attributed to species other than  $C^{5+}$ . Early Suzaku results show strong emission at low energies, due to a whole forest of unresolved lines of those species (G. V. Brown et al. 2007, private communication).

We performed an experiment using theoretical line strengths from a model by Koutroumpa et al. (2009). In this experiment, we extended the model down to 250 eV and added Mg VIII–X lines. The results of this had minimal effect on the measured C v flux but indicated a missing low energy component. Following this, we performed a similar experiment using Si VIII–X lines. The effect was dominated by Si IX (263 eV) and demonstrated a 25% reduction in measured C v flux while matching the observed low energy distribution. In a third experiment, we held the carbon C v line fixed at a flux level consistent with the observed solar wind and allowed the Mg lines to vary. The resultant  $\chi^2$  of the new fit was poorer, but by less than  $1\sigma$  than our nominal fit. We obtained a similar result using the low-lying excitation lines of Mg. This indicates that several factors may be in play to produce the relatively high measured flux of the C v line. These factors include the existence of poorly understood lines in this regime, the relatively low effective area below the carbon edge, and the relatively poor calibration of *Chandra* below 275 eV. However, there are neither enough data nor leverage below 310 eV to reliably distinguish C v from Si VIII–X, Mg VIII–X, or any other moderately strong ionic feature.

#### 4.3.3. Spectral Morphology

The defining characteristics of the global X-ray spectra of a comet are the velocity and state of the solar wind as well as the collisional opacity thickness of the comet. The latter of

these depends on  $Q_{\text{gas}}$  and drops as the distance from the comet cubed. It is not possible to tell solely from the global ionic ratios whether a comet was collisionally thick or thin, simply because elemental and ionic abundances in the solar wind are highly variable and the initial wind conditions could have been anything.

We can compare the results of the spectra in the shells of increasing radii using the CXE model (Bodewits et al. 2006, 2007). The interaction model assumes solar wind ions penetrating a neutral coma described by the Haser model. The Haser model assumes that a comet with a production rate  $Q$  has a spherically expanding neutral coma (Haser 1957; Festou 1981). The lifetime of neutrals in the solar radiation field varies greatly amongst species typical for cometary atmospheres (Huebner et al. 1992). The dissociation and ionization scale lengths also depend on absolute UV fluxes and therefore on the distance to the Sun. The coma is assumed to interact with solar wind ions, penetrating from the Sunward side following straight-line trajectories. The CXE processes between solar wind ions and coma neutrals are explicitly followed in both the change of the ionization state of the solar wind ions and the relaxation cascade of the excited ions. A three-dimensional integration, assuming cylindrical symmetry around the comet–Sun axis, finally yields the absolute intensity of the emission lines. Effects due to the observational geometry (i.e., FOV and phase angle) are included at this step in the model. There are likely to be other, minor effects, not included in the model. For example, the lifetime against photodissociation also depends strongly on solar activity because of the variation in  $Ly\alpha$ . At high solar activity, not only are the lifetimes of  $H_2O$  and  $OH$  considerably shortened, the dissociation also leads to a higher proportion of excess energy and thus more high-velocity H.

The CXE processes between solar wind ions and coma neutrals are explicitly followed in both the change of the ionization state of the solar wind ions and the relaxation cascade of the excited ions. Bodewits et al. (2006) calculated the effect on line ratios due to the distance from the comet center for  $Q_{\text{gas}}$  rates of  $10^{28}$  and  $10^{29}$  mol  $s^{-1}$  and a constant solar wind velocity of 450 km  $s^{-1}$ . For the most part, they found that the various line ratios are fairly flat for the low  $Q_{\text{gas}}$  case with stronger monotonic trends expected in the cases of  $O^{VIII}/O^{VII}$ ,  $C^{VI}/O^{VII}$ , and  $C^{VI}/C^{V}$ .

In Figure 11, we plot the observed trends for  $O^{VIII}/O^{VII}$  and  $C^{VI}/O^{VII}$  as a function of the distance from the peak of the emission. The solid line in these figures is linear least-squares fits, weighted by the measurement errors. The fits show a two-fold decrease in  $O^{VIII}/O^{VII}$ , as well as a similar increase in  $C^{VI}/O^{VII}$  over a span of about 20,000 km. These results are very close to the predictions given by Bodewits et al. (2007; Figure 7) for a low  $Q_{\text{gas}}$  comet with a modest (500 km  $s^{-1}$ ) wind. The ratio of  $C^{VI}/C^{V}$  is seen to rise as well, again consistent with the prediction of Bodewits et al. due to decreases in the density of the neutral gas further from the comet.

It must be noted that there are several caveats to this analysis. Errors on our observed ratios are fairly high, especially for small values of the radial distance from the nucleus. Figure 11 shows fits to the  $O^{VIII}/O^{VII}$  and  $C^{VI}/O^{VII}$  data as a function of distance from the peak of the emission near the center of the triangle. The data were fitted with error bars only for the ratios; the errors do not account for the positional issue that the emitting particles vary in their distance from the center and are not all at the mean distance—due to projection effects. Nonetheless, the formal probability that the obtained fit is consistent with

<sup>15</sup> <http://cxc.harvard.edu/cal/>.

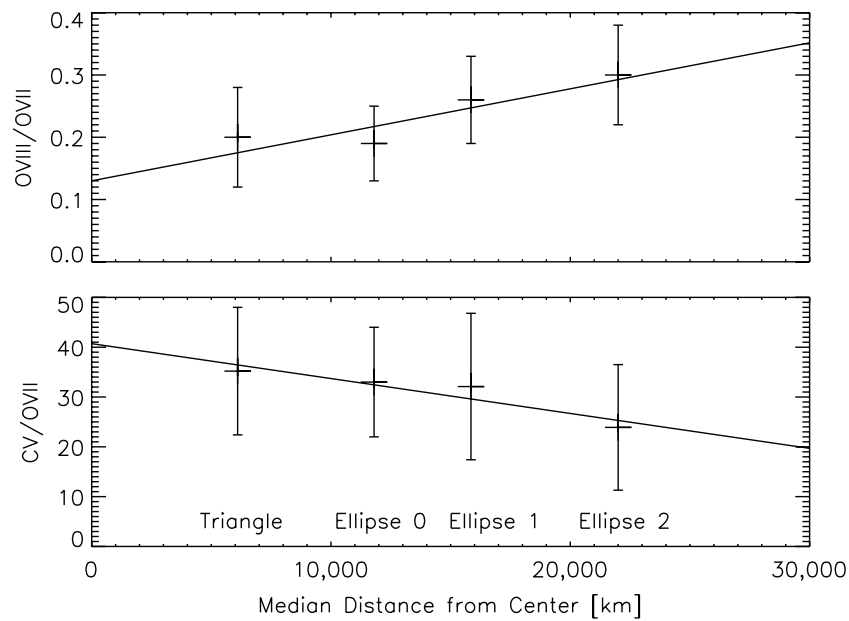


**Figure 11.** Trends in the ionization ratios measured in the emission lines vs. distance from the comet’s nucleus. The top figure shows O VIII/O VII, the bottom C V/O VII. Formal errors are included in the ratios. The X-axis shows the median distance of the measured points to the center of the “triangle” region. The straight lines are fitted to the data weighted by the errors in the measured ratios. O VIII/O VII is seen to increase with an increasing distance while C V/O VII decreases.

the correct model is about 90%. Moreover, while errors on our observed ratios are fairly high, especially close to the center of the emission, we note that if adjacent regions are combined, the errors shrink in quadrature and the extremal difference, that is, the significance of the trend, becomes  $\sim 3\sigma$ . Further, as discussed in the previous section, the C V line is highly contaminated by low-lying lines. So the changes observed in this feature may not be entirely due to a relative strengthening of the C V feature toward the center of the emission, but rather a strengthening of the composite of C V and the lower energy Si VIII–X and Mg VIII–X features.

In terms of flux, Ellipse 0 is the region of primary emission and accounts for about 65% of the total flux measured in the larger emitting region. The “triangle” represents an intensity enhancement within this inner ellipse accounting for about one-third of its flux in about one-fifth of the area. The two-fold decrease in O VIII/O VII as well as the similar increase in C V/O VII, may imply that the triangle of emission is brighter than its surrounding by 20% due to a slight density enhancement in the local coma neutral population. The low signal to noise of the data prevents a definitive statement in this regard, however.

#### 4.4. Optical versus X-ray Luminosity

In an early intercomparison among comets observed in the X-ray comparing the  $L_x/L_{\text{opt}}$  ratio served as an argument that whatever is causing the X-rays must be related to the gas and not to the dust in the cometary coma. For this purpose, Dennerl et al. (1997) introduced three bins for the gas-to-dust ratio. Within this binning, the  $L_x/L_{\text{opt}}$  ratio appears correlated with  $Q_{\text{gas}}/Q_{\text{dust}}$ .  $L_x$  was found to follow  $Q_{\text{gas}}^{0.67}$  for low  $Q_{\text{gas}}$  ( $L_{\text{opt}} < 10^{19.5}$ ). At higher values of  $Q_{\text{gas}}$  there was an apparent asymptote, with  $L_x$  never exceeding about  $10^{16}$  erg s $^{-1}$ .

There were (and still are) considerable uncertainties in the determination of both quantities (in particular, due to the temporal variability of  $L_x$ ), but there was also such a considerable dynamic range (3–4 orders of magnitude) for the “ROSAT comets” in  $L_x$  and  $L_{\text{opt}}$  that such a plot, with just three  $Q_{\text{gas}}/Q_{\text{dust}}$  bins, was

justified. We now know that CXE is the reason for the cometary emission; there is no longer any need to demonstrate that the gas in the cometary coma is the target for this interaction. In addition, there have been observed cases where  $L_x$  was highly variable, but neither  $L_{\text{opt}}$  nor  $Q_{\text{gas}}/Q_{\text{dust}}$  varied (e.g., Tempel 1 preimpact—Lisse et al. 2007; Encke—Lisse et al. 1999). So it is clear that the connection between  $L_x$  and the visual observables is not *always* directly related. In fact, we know that the type of the solar wind is an independent parameter that influences  $L_x$  independent of the comet (e.g., Bodewits et al. 2007). Finally, comets have been observed by various satellites (with different FOVs, different spectral coverage, different background), which makes a comparison of  $L_x$  a nontrivial task.

However, now that the asymptotic behavior has been explained as a collisional opacity effect (Lisse et al. 2004; Wegmann et al. 2004), such a plot should have renewed usefulness in distinguishing collisionally thin from collisionally thick systems. Indeed, limiting behaviors are seen in these data. The left-hand linear branch in Figure 12 is inhabited by faint, low activity comets and is explained by collisional depth. The basic explanation is as a comet has a larger gas production rate, the area over which it emits X-rays becomes larger, too. The surface brightness becomes lower, but the overall brightness increases roughly linearly with the outgassing rate. The turnover at  $L_x \sim 10^{16}$  ergs s $^{-1}$  is taken to indicate an intrinsic size limit for the neutral coma set by the ionization time for the majority coma species, such as H $_2$ O, CO, and CO $_2$  ( $\leq 10^6$  s), and the gas outflow rate (less than 1 km s $^{-1}$ ). This sets the intrinsic size limit for X-ray emission from any comet at about  $10^6$  km. The right side of the plot has more scatter and is occupied by high activity, X-ray bright comets.

To calculate luminosities, we measured fluxes from 0.30 to 1.0 keV using the CXE model with solar wind velocities from Bodewits et al. (2007) for each comet given in that paper. Temple 1 and Encke (2003) lie very close to Encke (1997), a low activity comet. Q4 (Neat) was very active, and moderately X-ray bright ( $\sim 3.4 \times 10^{15}$  erg s $^{-1}$ ), and lies near Hyakutake in the middle right of Figure 12. As noted previously, the flux from 73P/B was

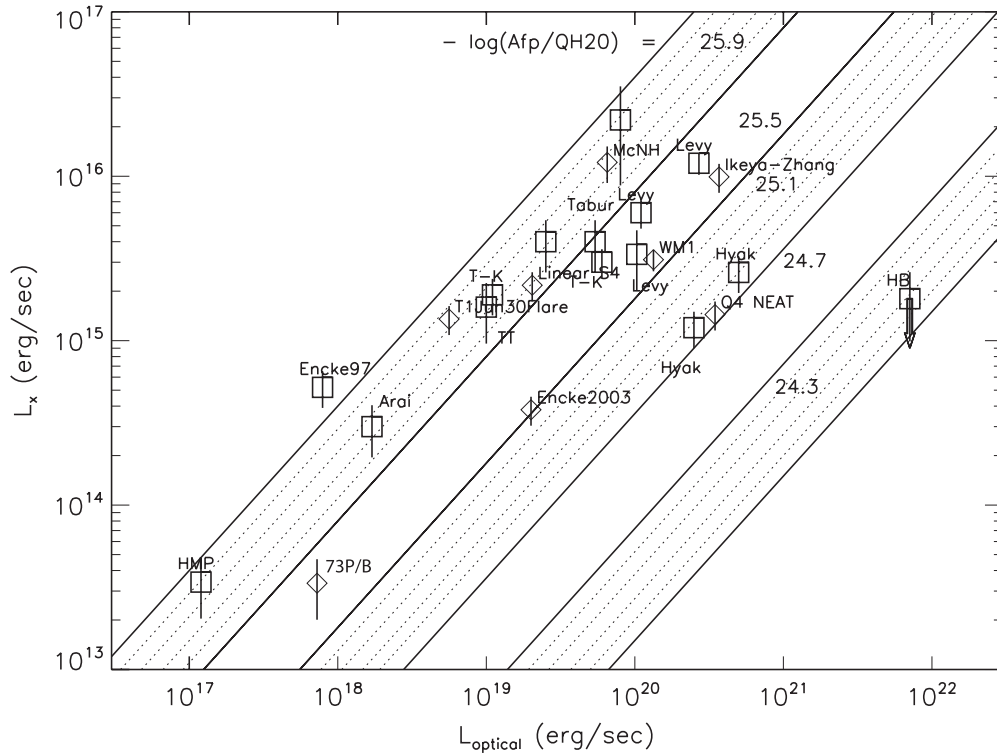


**Figure 12.** Plot of the X-ray vs. optical luminosity for about 15 comets. The diagonal lines represent constant dust-to-gas ratios for a comet observed with *ROSAT* until 1997. *Chandra*-observed comets are shown with diamonds; other X-ray-observed comets are shown with squares. The typical uncertainty of 0.2 mag ( $2\sigma$ ) in the optical flux translates to an uncertainty of  $\sim 20\%$  in  $L_{\text{optical}}$ . At lower X-ray luminosities comets seem to lie along a constant dust to gas ratio. X-ray luminosities appear to reach a maximum around  $L_x \approx 10^{16} \text{ ergs s}^{-1}$ . The unexplained faintness of comets (Hyakutake, NEAT, Hale-Bopp) at very high D/G ratios may argue for a mechanism of X-ray attenuation, like CXE between solar wind ions and dust particles, that favors Auger electron emission instead of X-ray emission,

calculated from 0.31 to 1.0 keV to correct for concerns near the carbon edge of the *Chandra* High Resolution Mirror Assembly (HRMA). This has a pronounced effect on a soft comet as was 73P/B, but a much smaller effect (less than 10%) on the other comets in the sample. The total observed luminosity from 73P/B of  $2.3 \times 10^{13} \text{ ergs s}^{-1}$  as derived in Section 3 is consistent with the luminosity derived from  $Q_{\text{gas}} \approx 10^{28} \text{ mol s}^{-1}$  as well as the simple models of Cravens (1997). This is similar to  $Q_{\text{gas}}$  found in Section 4.3.3. For optical luminosities below  $10^{19} \text{ ergs s}^{-1}$  the observed cometary optical and X-ray luminosities track well:  $L_x \sim 10^{-4} L_{\text{opt}}$ . Tempel 1 and Encke (2003 perihelion) are very close to Encke (1997 perihelion), implying consistency between *ROSAT* and *Chandra* observations. All are low activity comets, in the CXE collisionally thin regime.

#### 4.5. When Comets Disintegrate

The X-ray morphology of cometary fragment 73P/B motivated us to re-examine observations of the *Chandra* observations of CXE X-ray emission from LS4 on 2004 August 1, after that comet's total breakup. This emission has been a puzzling mystery for quite some time, as no obvious nucleus was seen in the *Chandra* images, and simple estimates of the lifetime of gas produced during the breakup on 2000 July 23 indicated that there should have been no gaseous material left from the breakup event by the time of the 2000 August 1 observations. We argue here that the source of the gas was the remnant debris of the comet that continued to outgas, at least through the August 1 observations.

Comparison of the debris field seen in *HST* of LS4 after its catastrophic breakup in late 2000 July to the *HST* imagery of 73P/B in 2007 April (see Figure 2 of Weaver et al. 2001) shows

an analogous structure, with a large concentration of fragments near the source nucleus and a fan of material spreading out as radiation pressure and Keplerian motion interact. We can thus expect that a triangular region of X-ray emission expanding toward the northeast could be seen for LS4 on 2000 August 1 by *Chandra*.

To obtain an X-ray spectrum of LS4 after breakup, we analyzed the 2001 August 1 observations of LS4 (proposal no. 01100323). This observation was taken about 1 week after the comet's breakup, and we used this to compare with the extended emission around 73P/B. Sixteen individual observations of LS4 were combined for a total exposure time of 18.6 ks. There was no obvious crescent-shaped comet in the LS4 S3 chip image. Rather, the image showed several discrete “knots” and possible diffuse emission (Figure 13). The total counts in the 300–1000 eV range on the S3 chip were 8430. This already indicates a fairly strong signal as there were only 6183 counts in that energy range detected on the S3 chip for 73P/B. The observation time was 18.6 ks for LS4 compared to 20.6 ks for 73P/B. Hence, LS4 was 50% brighter, despite being further away and completely disintegrated!

Figure 13 shows a highly smoothed image of the LS4 data in the 0.3–1.2 keV energy band. The Sun line and direction of motion are indicated, as is the location of a small grouping of greater than 70 m diameter fragments identified by Weaver et al. (2001). Their *HST* image is shown as the inset. The *HST* image clearly shows a broad fan of scattered light surrounding the big fragments, most likely due to fine dust (and most likely already gas depleted—because it is a fine dust of  $\sim 1 \mu\text{m}$  in size, with an outgassing lifetime of less than 1 day; Bockelée-Morvan et al. 2001). As for the fragments of 73P/B in the optical *HST* images, there appears to be a preference for the large debris to

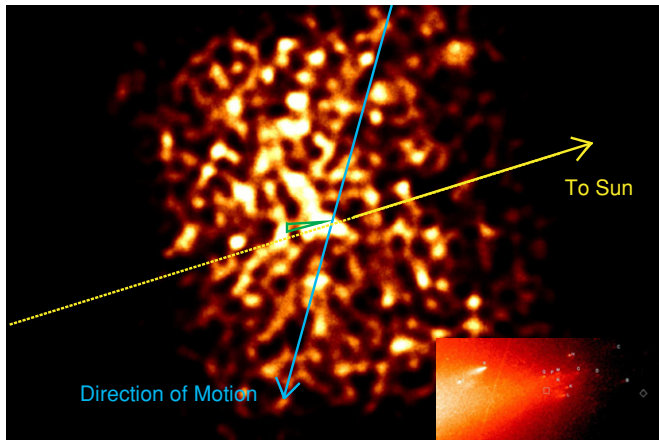


**Figure 13.** Smoothed image of CCD S3 from the observation of LS4 on 2000 August 1. In this image, north is up and east is to the left. Counts from energies between 0.3 and 1.2 keV are shown. Squared scaling is used. Data are binned and then smoothed using a Gaussian kernel; the final effective pixel size is  $\sim 13''$ . The Sun line (yellow) and direction of motion (cyan) are indicated, as is the location of a small grouping of large fragments ( $D > 70$  m), identified by Weaver et al. (2001; green triangle). The nominal nucleus position is the intersection of the vectors. Emission is brightest near the nominal location of the nucleus and in the (northeast) quadrant trailing the comet and away from the Sun. Inset: Figure 1 (middle) from Weaver et al. 2001. An *HST*/WFC image of LS4 taken in 2000 August 5. The diamond gives the predicted position of the original nucleus using the JPL-87 orbit solution and the square shows the predicted position of the nucleus using the JPL-95 orbit solution. Their separation is  $19''.3$ .

**Table 4**  
Total Counts in Various Regions of the LS4 FOV

Location	Area (arcsec)	Counts	Surface Brightness (counts pixel $^{-1}$ ) <sup>a</sup>	Error Surface Brightness (counts pixel $^{-1}$ ) <sup>a</sup>
Nuclear position <sup>b</sup>	1963.5	169	21.52	1.655
Southeast quadrant <sup>b</sup>	9188.2	642	17.46	0.688
Northeast quadrant <sup>b</sup>	31071.3	2327	18.72	0.388
Northwest quadrant <sup>b</sup>	15109.2	886	14.67	0.493
Southwest quadrant <sup>b</sup>	21116.3	1399	16.56	0.443
Nuclear position <sup>c</sup>	1963.5	80	10.19	1.140
Southeast quadrant <sup>c</sup>	9188.2	353	9.60	0.510
Northeast quadrant <sup>c</sup>	31071.3	1357	10.97	0.298
Northwest quadrant <sup>c</sup>	15109.2	589	9.75	0.403
Southwest quadrant <sup>c</sup>	21116.3	897	10.62	0.335

**Notes.**

<sup>a</sup>  $\times 10^{-3}$ .

<sup>b</sup> Energy range of 0.3–1.2 keV.

<sup>c</sup> Energy range of 1.2–2.2 keV.

be scattered in the antisolar direction (the triangle in Figure 13). Note that this comet was 5.5 times further away than 73P/B. If LS4 had been observed at the distance of 73P/B then the solid debris would have covered the entire CCD. The forces on small ice particles are dominated by solar radiation pressure and hence driven in the northeast quadrant of Figure 13, trailing the nucleus and away from the solar radiation vector.

The brightening is quantified in Table 4. The nominal nucleus is still the brightest region ( $0.086 \pm 0.007$  counts  $''^{-2}$ ). However the northeast quadrant is still quite bright ( $0.075 \pm 0.001$  counts  $''^{-2}$ ). This is about  $10 \sigma$  higher than the other three quadrants (average  $0.065 \pm 0.001$  counts  $''^{-2}$ ). When we examine the photon distribution at energies where we expect a very limited CXE signal (between 1200 eV and 2200 eV), we find that the northeast quadrant has  $0.044 \pm 0.001$  counts  $''^{-2}$  while

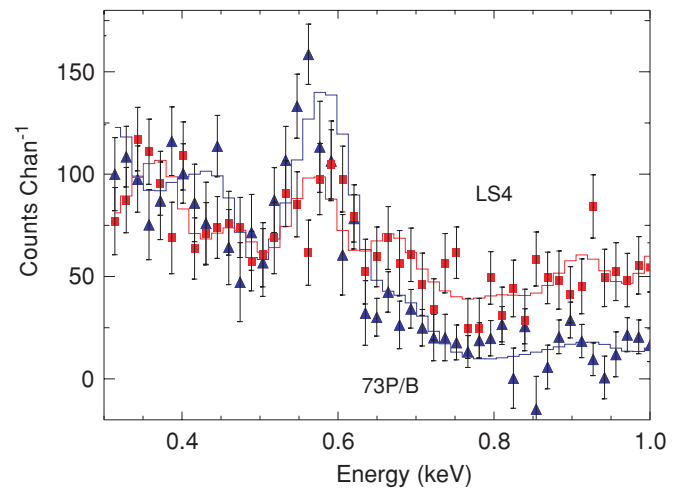


**Figure 14.** Spectra of LS4 (red squares) and 73P/B (blue triangles) from 0.3 to 1.0 keV. LS4 shows stronger C VI, O VIII, and Ne IX, (0.37, 0.65, and 1.02 keV, respectively) than 73P/B despite the fact that it had ceased to exist as a unique body over a week earlier.

the other three quadrants average  $0.041 \pm 0.001$  counts  $''^{-2}$ . While this is a  $3\sigma$  detection of excess it may be accounted for by high lying CXE lines, related to highly charged Fe, Si, and Mg ions, as observed during the interaction between comet Ikeya-Zhang and a CME (Bodewits et al. 2007; K. Dennerl et al. 2009, in preparation). Overall, this indicates that the excess background in the S3 chip observed at low energy was of astrophysical origin, that is, outgassing of cometary debris.

A spectrum was produced between 300 and 1000 eV in a  $225''$  radius circular aperture containing about 6500 counts and following the same prescription discussed in Section 2.3. Figure 14 shows both stronger carbon and neon emission by LS4 after its disintegration than seen in the extant comet 73P/B. As discussed in Section 4.2, the spectral structure depends primarily on the composition and ionization of the solar wind and secondarily on the density of the gas. In both cases, the cometary gas was optically thin to the CXE lines and the solar wind speeds are nearly identical ( $\sim 450$  km  $s^{-1}$  for LS4). However, LS4 was observed during solar maximum and the more highly ionized species, O VII and especially O VIII, dominated the solar wind. Hence, the shape of its spectrum is not too different from the prebreakup spectrum (Lisse et al. 2001). The key distinction appears to be the solar wind ionization state; LS4 has a “hot” spectrum while 73P/B has a colder spectrum.

## 5. CONCLUSIONS

On 2006 May 23, we observed comet 73P/2006 (Fragment B) for about 20 ks. At that point, the comet was closer to the Earth than any comet yet detected in X-rays. 73P/B was 0.97 AU from the Sun and 0.1 AU from the Earth, with a total visual magnitude of  $V \sim 7.5$  (Figure 2) and a total luminosity of  $L_{\text{optical}} \sim 7.25 \times 10^{17}$  erg  $s^{-1}$ . At the time of the observation, the fragment was relatively active, approximately the same brightness as the primary “C” fragment. The main difference between this comet and previous comets observed by *Chandra* was that its geocentric distance at the time of observation was extremely small, allowing for nearly in situ measurements of the solar wind by near-Earth satellites. The *Chandra* observations, folded through the models of Bodewits et al. (2007b) were consistent with the  $C^{6+}/O^{7+}$  ratio observed by *ACE*/SWICS. However, the  $C^{5+}/O^{7+}$  ratios were highly discrepant. Since we

cannot attribute the discrepancy to deficiencies in our knowledge of the  $C^{5+}$  cross sections, the *Chandra* calibration, or differences in the local solar wind, we are left to conclude that numerous additional species close in energy (200–300 eV) to C v have contaminated our spectral analysis. Future observations with a microcalorimeter are required in order to get a satisfactory understanding of this problem. In addition, the results of this work show the following.

1. The X-ray count rate from 73P/B was very stable—within 10% of  $0.0045 \pm 0.0015$  counts  $s^{-1}$ .
2. The overall morphology of the emission is roughly elliptical, with the triangular concentration within the ellipse of emission. One side of the triangle is aligned with the direction of orbital motion; the other is aligned with the Sun. This morphology can be understood as symmetric, emission dominated by several large pieces of 73P/B moving close to the comet's orbital path. The composite of these fills the triangle with Sunward emission.
3. The X-ray flux from the entire comet “bigbox” between 0.31 and 1.0 keV was about  $8.0 \times 10^{-13}$  ergs  $cm^{-2} s^{-1}$ . This is a luminosity of  $2.3 \times 10^{13}$  ergs  $s^{-1}$ . About 25% of the flux comes from a small triangular region located forward of the nucleus relative to the direction of motion. This region is about 20,000 km on a side.
4. The spectrum of the comet is well fitted by a CXE model containing four species each of two ions—C, N, O, and Ne—and an observed solar wind speed of about 450 km  $s^{-1}$ . Comparison of the line fluxes with the ionic ratios in the solar wind raises concerns that the flux attributed to C v may not be entirely due to C v. Lines lying below the nominal 300 eV cutoff of the HRMA+ACIS system may be contributing to the measured flux. We are encouraged that work on identifying possible contributors to these lines is being actively pursued.
5. Following Bodewits et al. (2007), comet 73P/B interacted with the cold-fast solar wind. This is a reflection of the solar wind being relatively fast, but the ionization fraction in the solar wind of O VIII/O VII was very low—the lowest observed in the *Chandra* era—despite some evidence of mixing with the CIR.<sup>16</sup> The cold ionization state means that ionized oxygen in the solar wind is preferentially O VI and not O VII or O VIII. This is one reason why the X-ray luminosity is low—the CXE-driven emission from O VI maybe primarily in the EUV. Comet 73P/B is, spectrally, very similar to the observation of comet 2P/Encke 2003.
6. We analyzed the spectrum as a series of elliptical annuli and found that the line ratios of O VIII/O VII (653/561 eV) and C VI/C V (367/299 eV) decrease as one moves from the outer regions of the comet toward the peaks of the emission. Meanwhile, C V/O VIIg (299/561 eV) increases as one moves from the outside in. While the individual measurements have  $\sim 30\%$  errors, the trend is significant beyond the  $3\sigma$  level. This is confirmation of the predictions of Bodewits et al. (2007) of the behavior of emission ratios within a collisionally thin medium undergoing CXE.
7. Despite its ongoing breakup, 73P/B's luminosity is similar to other low activity ecliptic comets with  $L_X/L_{opt} \sim 10^{-4}$ .
8. The lower limit to the outgassing rate as determined by the observed flux intensity and comparison to Tempel 1/Deep Impact is at least  $3 \times 10^{27}$  mol  $s^{-1}$ . The true rate is probably

a factor of a few higher, but less than  $2 \times 10^{28}$  mol  $s^{-1}$  observed by Schleicher using narrowband photometry a week earlier.

9. Extending the morphological analysis, we can also understand the observation of LS4 in 2000 August. Smaller pieces of debris for this comet, influenced much more strongly by solar radiation pressure, caused the LS4 debris to preferentially occupy the region northeast of the nominal position of the (former) nucleus. This would have been classified as a hot-fast solar wind comet. Hence, LS4 postbreakup showed stronger C VI, O VIII, and Ne IX than 73P/B.

We thank H. Tananbaum for use of Director's Discretionary time for this unusual object. We thank D. Koutroumpa and V. Kharchenko for helpful discussions on the C v contamination issue. We are grateful for the cometary ephemerides of D. K. Yeomans published at the JPL/Horizons Web site. Proton velocities and ion measurements used here are courtesy of the *SOHO/CELIAS/PM* and *ACE/SWICS* teams, respectively. The CXC guest investigator program supported this work through grants DD6-7040X (S.J.W.) and GO4-5167X (C.M.L.). S.J.W. was supported by NASA contract NAS8-03060. D.B. wishes to acknowledge travel support from the Netherlands Organisation for Scientific Research (NWO), the High Energy Astrophysics Division at the Center of Astrophysics, and the Visiting Scholars Program of the Institute of Theoretical Atomic, Molecular and Optical Physics at the Center for Astrophysics.

## REFERENCES

- Arnaud, K. A. 1996, in ASP Conf. Ser. 101, *Astronomical Data Analysis Software and Systems V*, ed. G. Hunt & H. E. Payne (San Francisco, CA: ASP), 17
- Beiersdorfer, P., et al. 2003, *Science*, **300**, 1558
- Bhardwaj, A., et al. 2007, *Planet Space Sci.*, **55**, 1135
- Bockelée-Morvan, D., et al. 2001, *Science*, **292**, 1339
- Bodewits, D. 2007, PhD thesis, Univ. Groningen, available online at <http://irs.ub.rug.nl/ppn/303146974>
- Bodewits, D., Hoekstra, R., Serebryuk, B., McCullough, R. W., Jones, G. H., & Tielens, A. G. G. M. 2006, *ApJ*, **642**, 593
- Bodewits, D., Juhász, Z., Hoekstra, R., & Tielens, A. G. G. M. 2004, *ApJ*, **606**, L81
- Bodewits, D., et al. 2007, *A&A*, **469**, 1183
- Bohnhardt, H., Kaufl, H. U., Keen, R., Camilleri, P., Carvajal, J., & Hale, A. 1995, *IAU Circ.*, 6274, 1
- Boney, B. P., Mumma, M. J., Kawakita, H., Kobayashi, H., & Villanueva, G. L. 2008, *Icarus*, **196**, 241
- Burns, J. A., Lamy, P. L., & Soter, S. 1979, *Icarus*, **40**, 1
- Cravens, T. E. 1991, in *Comets in the Post-Halley Era*, ed. R. L. Newburn, Jr. et al. (Dordrecht: Kluwer), 1211
- Cravens, T. E. 1997, *Geophys. Res. Lett.*, **24**, 105
- Cravens, T. E. 2002, *Science*, **296**, 1042
- Dello Russo, N., Vervack, R. J., Weaver, H. A., Biver, N., Bockelée-Morvan, D., Crovisier, J., & Lisse, C. M. 2007, *Nature*, **448**, 172
- Dennerl, K. 2002, *A&A*, **394**, 1119
- Dennerl, K., Englhauser, J., & Trümper, J. 1997, *Science*, **277**, 1625
- Festou, M. C. 1981, *A&A*, **95**, 69
- Flammer, K. R. 1991, in *Comets in the Post-Halley Era*, ed. R. L. Newburn, Jr. et al. (Dordrecht: Kluwer), 1125
- Galeev, A. A., Gribov, B. E., Gringauz, K. I., Klimov, S. I., & Gombosi, T. 1986, *Geophys. Res. Lett.*, **13**, 841
- Gringauz, K. I., et al. 1986, *Nature*, **321**, 282
- Haser, L. 1957, *Bull. Soc. R. Sci. Liege*, **43**, 740
- Horanyi, M., & Mendis, D. A. 1986, *J. Geophys. Res.*, **91**, 355
- Horanyi, M., & Mendis, D. A. 1991, *The Electrodynamics of Charged Dust in the Cometary Environment*, IAU Coll. 116: *Comets in the Post-Halley Era* 167, ed. R. L. Newburn, M. Neugebauer, & J. Rahe (Dordrecht: Kluwer), 1093
- Huebner, W. F., Keady, J. J., & Lyon, S. P. 1992, *Ap&SS*, **195**, 1

<sup>16</sup> Comet 17P/Holmes, observed in 2007 November, may have been immersed in an even colder solar wind. These data are still being analyzed.

- Ip, W.-H. 2004, *Global Solar Wind Interaction and Ionospheric Dynamics, Comets, II*, ed. M. C. Festou, H. U. Keller, & H. A. Weaver (Tucson, AZ: Univ. Arizona Press), 605
- Johnstone, A. D., et al. 1993, *A&A*, 273, L1
- Kabin, K., et al. 2000, *Ap&SS*, 274, 407
- Kharchenko, V., & Dalgarno, A. 2000, *J. Geophys. Res.*, 105, 18351
- Kharchenko, V., & Dalgarno, A. 2001, *ApJ*, 554, L99
- Koutroumpa, D., Lallement, R., Kharchenko, V., & Dalgarno, A. 2009, *Space Sci. Rev.*, 143, 217
- Krankowsky, D., et al. 1986, *Nature*, 321, 326
- Krasnopolsky, V. A., Christian, D. J., Kharchenko, V., Dalgarno, A., Wolk, S. J., Lisse, C. M., & Stern, S. A. 2002, *Icarus*, 160, 437
- Krasnopolsky, V. A., Mumma, M. J., Abbott, M., Flynn, B. C., Meech, K. J., Yeomans, D. K., Feldman, P. D., & Cosmovici, C. B. 1997, *Science*, 277, 1488
- Küppers, M., et al. 2005, *Nature*, 437, 987
- Lisse, C. M., A'Hearn, M. F., Hauser, M. G., Kelsall, T., Lien, D. J., Moseley, S. H., Reach, W. T., & Silverberg, R. F. 1998, *ApJ*, 496, 971
- Lisse, C. M., Christian, D. J., Dennerl, K., Meech, K. J., Petre, R., Weaver, H. A., & Wolk, S. J. 2001, *Science*, 292, 1343
- Lisse, C. M., Cravens, T. E., & Dennerl, K. 2004, *X-Ray and Extreme Ultraviolet Emission from Comets, Comets, II*, ed. M. C. Festou, H. U. Keller, & H. A. Weaver (Tucson, AZ: Univ. Arizona Press), 631
- Lisse, C. M., et al. 1996, *Science*, 274, 205
- Lisse, C. M., et al. 1999, *Icarus*, 141, 316
- Lisse, C. M., et al. 2005, *ApJ*, 625, L139
- Lisse, C. M., et al. 2007, *Icarus*, 190, 391
- Mazzotta, P., Mazzitelli, G., Colafrancesco, S., & Vittorio, N. 1998, *A&AS*, 133, 403
- McCammon, D., et al. 2002, *ApJ*, 576, 188
- Neugebauer, M., et al. 2000, *J. Geophys. Res.*, 105, 20949
- Pepino, R., Kharchenko, V., Dalgarno, A., & Lallement, R. 2004, *ApJ*, 617, 1347
- Reach, W. T., Kelley, M. S., & Sykes, M. V. 2007, *Icarus*, 191, 298
- Reach, W. T., Sykes, M. V., Lien, D., & Davies, J. K. 2000, *Icarus*, 148, 80
- Reach, W. T., et al. 2006, *AJ*, 131, 1479
- Sasseen, T. P., Hurwitz, M., Lisse, C. M., Kharchenko, V., Christian, D., Wolk, S. J., Sirk, M. M., & Dalgarno, A. 2006, *ApJ*, 650, 461
- Schleicher, D. 2006, *Central Bur. Electron. Telegrams*, 491, 1
- Schwadron, N. A., & Cravens, T. E. 2000, *ApJ*, 544, 558
- Villanueva, G. L., Bonev, B. P., Mumma, M. J., Magee-Sauer, K., DiSanti, M. A., Salyk, C., & Blake, G. A. 2006, *ApJ*, 650, L87
- Weaver, H. A., Lisse, C. M., Mutchler, M. J., Lamy, P., Toth, I., & Reach, W. T. 2006, *BAAS*, 38, 490
- Weaver, H. A., et al. 2001, *Science*, 292, 1329
- Wegmann, R., & Dennerl, K. 2005, *A&A*, 430, L33
- Wegmann, R., Dennerl, K., & Lisse, C. M. 2004, *A&A*, 428, 647
- Young, D. T., et al. 2004, *Icarus*, 167, 80
- Zurbuchen, T. H., Fisk, L. A., Gloeckler, G., & von Steiger, R. 2002, *Geophys. Res. Lett.*, 29, 090000